Contourite channels – Facies model and channel evolution

WOUTER DE WEGER* (iD), F. JAVIER HERNANDEZ-MOLINA*,
FRANCISCO JAVIER SIERRO†, DOMENICO CHIARELLA* (iD), ESTEFANIA LLAVE‡ (iD),
JUAN J. FEDELE§, FRANCISCO JAVIER RODRIGUES-TOVAR¶ (iD),
OLMO MIGUEZ-SALAS¶ and MOHAMED AMINE MANAR**

*Department of Earth Sciences, Royal Holloway, University of London, Egham, Surrey, TW20 0EX, UK
(E-mail: wouter.deweger.2017@live.rhul.ac.uk)
†Departament de Geologia, Universidad de Salamanca, Plaza de los Caídos, Salamanca, 37008, Spain
‡Instituto Geologico y Minero de España (IGME), C/Rios Rosas, 23, Madrid, 28003, Spain
§ExxonMobil Upstream Research Company, 22777 Springwoods Village Parkway Spring, Houston, TX, 77389, USA
¶Departamento de Estratigrafía y Paleontología, Universidad de Granada, Avd. Fuentenueva s/n, 18002, Granada, Spain
**Office National des Hydrocarbures et de Mines (ONHYM), 34, Avenue Al Fadila, Rabat, BP 99, Morocco

ABSTRACT

Despite the rise in published evidence of deep-marine bottom current processes and associated deposits there are still very few documented outcrop examples. Herein are reported results of a contourite channel system related to the late Miocene palaeo-Mediterranean Outflow Water in the Rifian Corridor, Morocco. This work aims to unravel the sedimentary evolution and facies distribution based on the study of large morphological features related to contourite channels and their subsequent sandstone dominated infill sequences. It was found that the channel evolution and facies distribution are related to spatiotemporal changes in flow characteristics of the palaeo-Mediterranean Outflow Water. The recognized channel facies distribution correlates well with previously established bedform stability diagrams. Erosion and upper-stage flow regime bedforms are associated with the most vigorous bottom currents, generally related to its core. Laterally, following the decrease in flow velocity towards the adjacent drift, bedforms comprise dunes, lower-stage plane bedforms and more heterolithic facies. Similar facies changes are also observed down-channel, related to a decrease in flow velocities resulting from turbulent mixing of water masses, associated decreases in density gradients and the subsequent deceleration due to gravity. Results of this work have been used to propose a three-dimensional facies model for channelized sandy contourites. This study contributes to understanding contourite systems, thus benefitting oceanographic and climatic reconstructions as well as aiding the predictability of contourite channel systems for industry geoscience applications.

Keywords Bottom currents, contourite channel system, contouritic drifts, deep-water sedimentation, facies models, Late Miocene, Morocco, Rifian Corridor, tides.

INTRODUCTION

Many depositional processes in the deep-marine realm, particularly with regard to bottom currents are not well-understood. This has led to a bias in assumptions towards processes that gained more scientific attention. As such, the poorly understood hydrodynamic behaviour of bottom currents and their depositional processes hinders the recognition of contourites (de Weger *et al.*, 2021), hampering their scientific attention.

Over the last decades there has been a significant rise in published evidence of deep-marine bottom current processes and associated deposits. Most of these works are based on seismic data (Faugères *et al.*, 1999; Rebesco *et al.*, 2014; Paulat *et al.*, 2019), some from wells and cores (Gonthier *et al.*, 1984; de Castro *et al.*, 2020, 2021; Hovikoski *et al.*, 2020), but there is still very little information from the outcrop record (Duan *et al.*, 1993; de Weger *et al.*, 2021; Hüneke *et al.*, 2021). This is particularly true for deep-water contourite channels.

Significant advances in the sedimentological understanding of deep-water channels and their sedimentary features have been made in recent years. These advances have mainly focused on channel belts and channel belt systems formed by down-slope gravity driven processes. These channels comprise architectural elements such as lateral-accretion packages, channel-bend mounds, levées, non-turbiditic mass-transport deposits and last-stage channel-fills (Walker, 1978; Weimer & Slatt, 2004; Kolla *et al.*, 2007; Wynn *et al.*, 2007; Harris & Whiteway, 2011; Janocko *et al.*, 2013; Peakall & Sumner, 2015). Contrastingly, contourite channels (Hernández-Molina *et al.*, 2006; García *et al.*, 2009) have received much less scientific attention. Moreover, the erosional contourite features have received much less scientific attention compared to the much larger contourite drift deposits. Contourite channels, however, might contain significant information on past and current ocean circulation, current behaviour and thus climate. Furthermore, their coarse-grained nature makes them valuable reservoir targets for hydrocarbon exploration or CO_2 sequestration and storage.

Attempts to better understand the sedimentological features of modern contourite channel systems by studying cores were generally unsuccessful because the sediment proved too unconsolidated for acquisition (Expedition 339 Scientists, 2012; Brackenridge *et al.*, 2018; de Castro *et al.*, 2021). As a result, the information from these features is generally limited to bathymetric remote sensing and direct imaging (Stow *et al.*, 2009, 2013). Observations from the ancient rock record are predominantly based on seismic data, cores and logs (Hernández-Molina *et al.*, 2014; Gong *et al.*, 2017). Because of the extreme differences in scale and resolution between these, comprehensive understanding and testing of process hypotheses relating the evolution of contourite erosive features and their associated infill deposits have remained elusive.

Herein is reported the results of an extensive field outcrop study of an exposed late Miocene contourite channel system in northern Morocco (Capella *et al.*, 2017, 2018; de Weger *et al.*, 2020, 2021). De Weger *et al.* (2020, 2021) recently described the occurrence and the regional evolution of these channels, but the lateral and vertical variations of sedimentary facies and depositional sequences within the channels had not yet been considered in detail. Therefore, the aims of this work are to: (i) improve general understanding of contourite channel systems, their sedimentary facies and depositional sequences; (ii) better understand the detailed hydrodynamic behaviour of channelized bottom currents; (iii) identify recognition criteria for sandy contourites; and (iv) propose a facies model for these systems. Finally, this contribution will address some of the implications for climatic studies and industry resource and exploration potential.

STUDY AREA AND GEOLOGICAL SETTING

The studied outcrops (i.e. *Sidi Chahed* and *Kirmta*) are exposed in the Rifian Corridor of northern Morocco (Fig. 1). This corridor is part of the external zone of the Rif–Betic-Arc, or Gibraltar-Arc which forms an arc-shaped orogenic belt surrounding the Alboran Sea in the westernmost Mediterranean region. The Rifian Corridor formed a late Miocene marine gateway that allowed Mediterranean–Atlantic water exchange (Capella *et al.*, 2017; Krijgsman *et al.*, 2018). The corridor evolved as a south-westward migrating foreland basin during the Tortonian (*ca* 8 Ma) (Feinberg, 1986; Wernli, 1988; Sani *et al.*, 2007), limited northward by the earlier exhumed Rif orogenic wedge (Iribarren *et al.*, 2009) and southward by the Middle Atlas

Fig. 1. Palaeogeographical reconstruction of the late Miocene Rifian Corridor, Morocco (modified after de Weger *et al.*, 2020, 2021). The Betic and Rif, Middle Atlas, Prerif Ridges and the Taza-Sill form the main geological features. The studied outcrops are related to different branches of the palaeo-Mediterranean Outflow Water (MOW). The small globe depicts the location of the study area, the general ocean circulation pattern and, in orange, the trajectory of the present-day MOW.
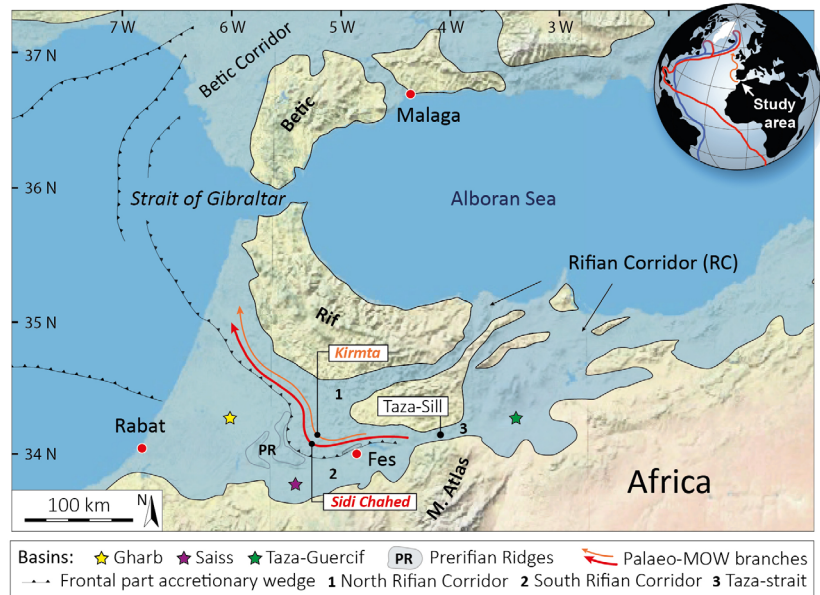
Mountains (Barbero *et al.*, 2011). The Rifian Corridor is divided into two strands (Fig. 1), the North Rifian Corridor related to the Intramontane Basins, and the South Rifian Corridor related to the Taza–Guercif and Saiss basins (Wernli, 1988). The strands were separated by the chaotic complex of the accretionary wedge, emplaced over the African foreland since the early Tortonian (Feinberg, 1986; Flinch *et al.*, 1996; Chalouan *et al.*, 2008; Michard *et al.*, 2008). Since the accretionary wedge is locally overlain by Upper Miocene marine sediments, the Rifian Corridor, at times, was a single wide gateway (Fig. 1) westward of the Taza-Sill (Flecker *et al.*, 2015; Capella *et al.*, 2017; de Weger *et al.*, 2020). During the late Tortonian to early Messinian the Prerif Ridges were formed, constituting a subaqueous relief (Fig. 1) in the South Rifian Corridor (Roldán *et al.*, 2014; de Weger *et al.*, 2020). By roughly 7.5 Ma these ridges were sufficiently uplifted to displace the contourite channel system described herein (de Weger *et al.*, 2021).

The Taza-Sill, located in the Taza Strait (de Weger *et al.*, 2021), formed a submerged topographic high related to the east–west oriented thrust-front overlying the north-east/south-west oriented Middle-Atlas (Fig. 1). The Taza Strait separated the Taza–Guercif and the Saiss basins and the Taza-Sill controlled the water-mass exchange between the Mediterranean and the Atlantic (Capella *et al.*, 2017; de Weger *et al.*, 2020, 2021). The westernmost part of the Rifian Corridor, just west of the Prerif Ridges, was in

the Gharb Basin (Fig. 1) where both the Intramontane, associated with the North Rifian Corridor and Saiss basins merged (Sani *et al.*, 2007).

PALAEOCEANOGRAPHIC SETTING

During the late Miocene an Atlantic – Mediterranean connection existed through the Betic Corridors in southern Spain and the Rifian Corridors in northern Morocco (Fig. 1). The Rifian Corridor likely represented the last remaining connection before the onset of the Mediterranean Salinity Crisis (MSC; 5.97–5.33 Ma, Hsü *et al.*, 1973; Ryan & Hsü, 1973). The MSC is associated with the restriction and closure of the Miocene Atlantic–Mediterranean connections which resulted in extreme salinity fluctuations in the Mediterranean. The full opening of the Strait of Gibraltar (5.33 Ma) brought the MSC to an end (Hsü *et al.*, 1973, 1977; Blanc, 2002; Garcia-Castellanos *et al.*, 2009; Krijgsman *et al.*, 2018).

After the restriction and closure of the Betic Corridors in the late Miocene (Flecker *et al.*, 2015), the Rifian Corridor maintained Atlantic–Mediterranean water exchange in a similar fashion to the present-day Strait of Gibraltar (de Weger *et al.*, 2020, 2021). The Rifian Corridor accommodated inflow of the North Atlantic Surficial Water and likely the Eastern North Atlantic Central Water into the Mediterranean, overriding the warm and highly saline palaeo-

Mediterranean Outflow Water (MOW). The water mass of the palaeo-MOW was formed by net evaporation in the eastern Mediterranean, which increased the density of Mediterranean surface water (Straume *et al.*, 2020). This surface water was 'continuously' replenished by the inflow of cold and less saline Atlantic water. Subsequently, the increase in density forced this water to sink and ventilate the water column, a process known as intermediate and deep-water formation (Millot, 1999; Candela, 2001). The formation of these relatively dense water masses resulted in a density gradient between the Mediterranean and the Atlantic which drove two-way exchange (Rohling *et al.*, 2015; Simon *et al.*, 2017). During the late Miocene, a dense palaeo-MOW flowed over the Taza-Sill (Fig. 1), through the Rifian Corridor, towards the Atlantic (de Weger *et al.*, 2020, 2021).

METHODOLOGY

Two well-exposed outcrops from the Rifian Corridor; Sidi Chahed and Kirmta (Figs 1 and 2), are studied herein. These outcrops were previously documented and interpreted as being relics of contourite channels (de Weger *et al.*, 2020). Here, contourite channels were studied in more detail to unravel erosional events that led to channel formation, their

evolution, and the vertical and lateral facies variability of their infill sequences.

The sedimentary record was studied by standard field techniques which include bed-scale characterization of sedimentological and stratigraphic elements. Twelve stratigraphic sections were measured at centimetre to metre-scale to document key features used in facies analyses. These features include lithology, grain size and sorting, sedimentary structures, bedding thickness, nature of bed contacts and palaeocurrent indicators. The sand fraction predominantly consists of a mixed bioclastic–siliciclastic composition for which the terminology proposed by Chiarella *et al.* (2017) is applied. A total of 323 observations of palaeoflow indicators (for example, cross-stratification, ripple-lamination and sole-marks) were recorded across both of the outcrops. In addition, high resolution photography taken during different seasons (winter and autumn of 2018 and spring of 2019) were used for detailed analyses of morphologies and facies distributions.

Fifteen samples for biostratigraphic determinations, collected from marls that were more than 50 cm below the rock's exposed surface, have been analysed and compared to the findings of Capella *et al.* (2017). The palaeo-water depth has been inferred from the benthic foraminifera assemblages of the biostratigraphic samples. The observed mixed occurrence of shallow-water
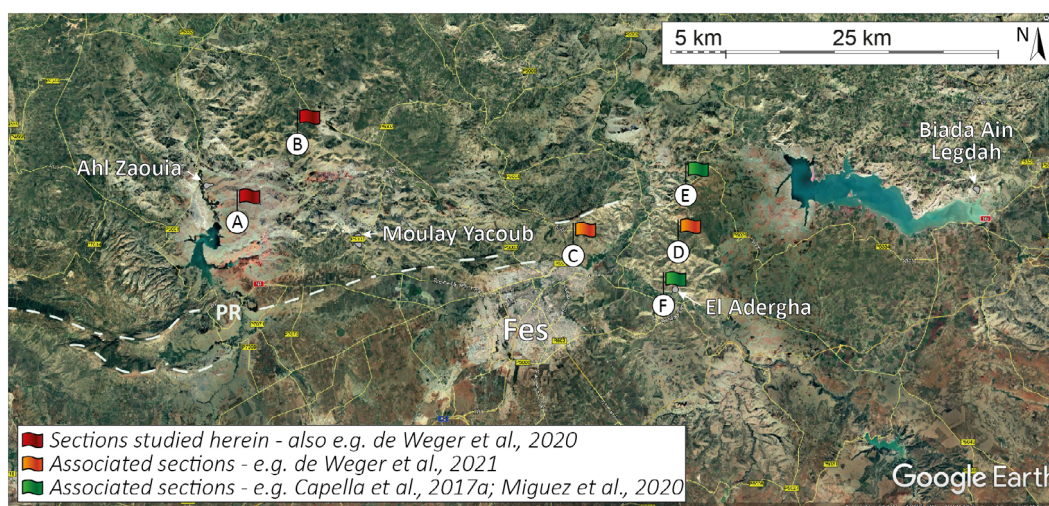

Fig. 2. Satellite image of the study area near the city of Fes. The main sections described herein, (A) Sidi Chahed and (B) Kirmta are located north of the Prerif Ridges (PR). The locations of Fes-north (C), El Adergha (D), Ain Kansera (E) and Sidi Harazem (F) sections, located south of the PR, are provided as a reference. These references contain further details.

and deep-water species is considered here the result of down-slope transport and, hence, the deeper-water species are deemed most reliable in depositional depth estimates.

Ichnological analysis was primarily conducted in the sand-rich facies of the studied sections. Ichnotaxonomy, distribution and abundance of trace fossils were characterized to describe stratigraphic trends and lateral and vertical variability to decode the environmental conditions during or after sedimentation. Ichnological observations focused on orientation, shape, length and diameter of individual burrow segments, configuration of burrow systems, relationship with facies and bed surfaces, and taphonomy.

Thirty-nine samples for petrographic analysis were collected from indurated sand beds. Two sets of thin sections were prepared for each sample, one of which was impregnated with dyed resin to highlight porosity. The samples were examined under a petrographic microscope with integral camera system. Modal analysis was carried out on five samples (BAT2a, BAT2b, BAT2c, BAT4 and BAT14) by determining the composition at 300 points using a stepping stage and associated PETROG™ software.

STUDIED SECTIONS

Both Sidi Chahed (Fig. 3A to I) and Kirmta (Fig. 4) were accumulated in wedge-top basins on the northern flank of the Saiss Basin. The outcrops are located *ca* 9 km apart (Fig. 2). The Sidi Chahed outcrop (34.102693, −5.299355) is located roughly 25 km WNW of the city of Fes and 5 km north of the Prerif Ridges. The Kirmta outcrop (34.171445, −5.239184) is located 22 km north-west of the city of Fes and 12 km north of the Prerif Ridges (Fig. 2).

The Sidi Chahed section forms a topographic high composed of three arcuate, indurated sandstone ridges which measure 2 km (east–west) by 1 km (north–south) (Fig. 3A). The southern, western and eastern flanks are typically steeply sloped to near vertically inclined. The northern flanks are much less inclined to near horizontal in places. The total thickness of the section, consisting of three concave-up sandstone units (SU1, SU2 and SU3) encased in marls and sandy marls belonging to the Blue Marl Formation is roughly 140 m (Fig. 3).

The Kirmta outcrop is roughly 110 m thick, forming a topographic high with three distinct sandstone units (SU1, SU2 and SU3) encased in marl and sandy marls belonging to the Blue Marl Formation (Fig. 4). The southern flank of the outcrop, which is exposed for well over 3 km, is steeply inclined whereas the northern flank hardly shows any inclination.

RESULTS

Distribution of channelized sandstone bodies and internal architectures

Both the Sidi Chahed and Kirmta outcrops consist of three sandstone units (SU1 to SU3) that are encased in fine-grained marl deposits. All sandstone units have concave-up geometries (Figs 3 and 4). The concave-up lower bounding surface of each sand unit, herein referred to as first-order channel, is in unconformable contact with fine-grained marl deposits. In the Sidi Chahed outcrop these first-order channels are 750 to 1000 m wide and up to 35 m thick (Fig. 3A to J), whereas in the Kirmta outcrop these first-order channels are up to 2 km wide and 5 to 15 m thick (Fig. 4). The first-order channels, most clearly observed in the Sidi Chahed outcrop, contain smaller concave-up sandstone bodies (Fig. 3J), herein referred to as second-order channels. These second-order channels are incised into previously deposited sandstones. The width of these second-order channels ranges between 30 m and 300 m and their thickness does not exceed 15 m.

Age and palaeo-water depth

The biostratigraphic results from the Sidi Chahed section indicate that the section was deposited within the *Globigerinoides obliquus extremus/Globorotalia suterae* biozone MMi-12a interval of Lirer *et al.* (2019). The lowermost part of the section, below the first sand unit (SU1), is dominated by sinistrally coiled *Neogloboguadrina acostaensis* and *Globorotalia scitula*, including specimens of *G. suterae* and *Globorotalia menardii 4*. This foraminifer assemblage suggests a late Tortonian age, younger than 7.80 Ma. The uppermost marlstones derived stratigraphically above the uppermost sand unit (SU3), showed an abundant presence of *G. menardii 4* and no presence of *G. menardi 5*, indicating that the whole succession was deposited prior to 7.51 Ma.

The benthic foraminiferal assemblages of the Sidi Chahed outcrop consist of mixed shallow-
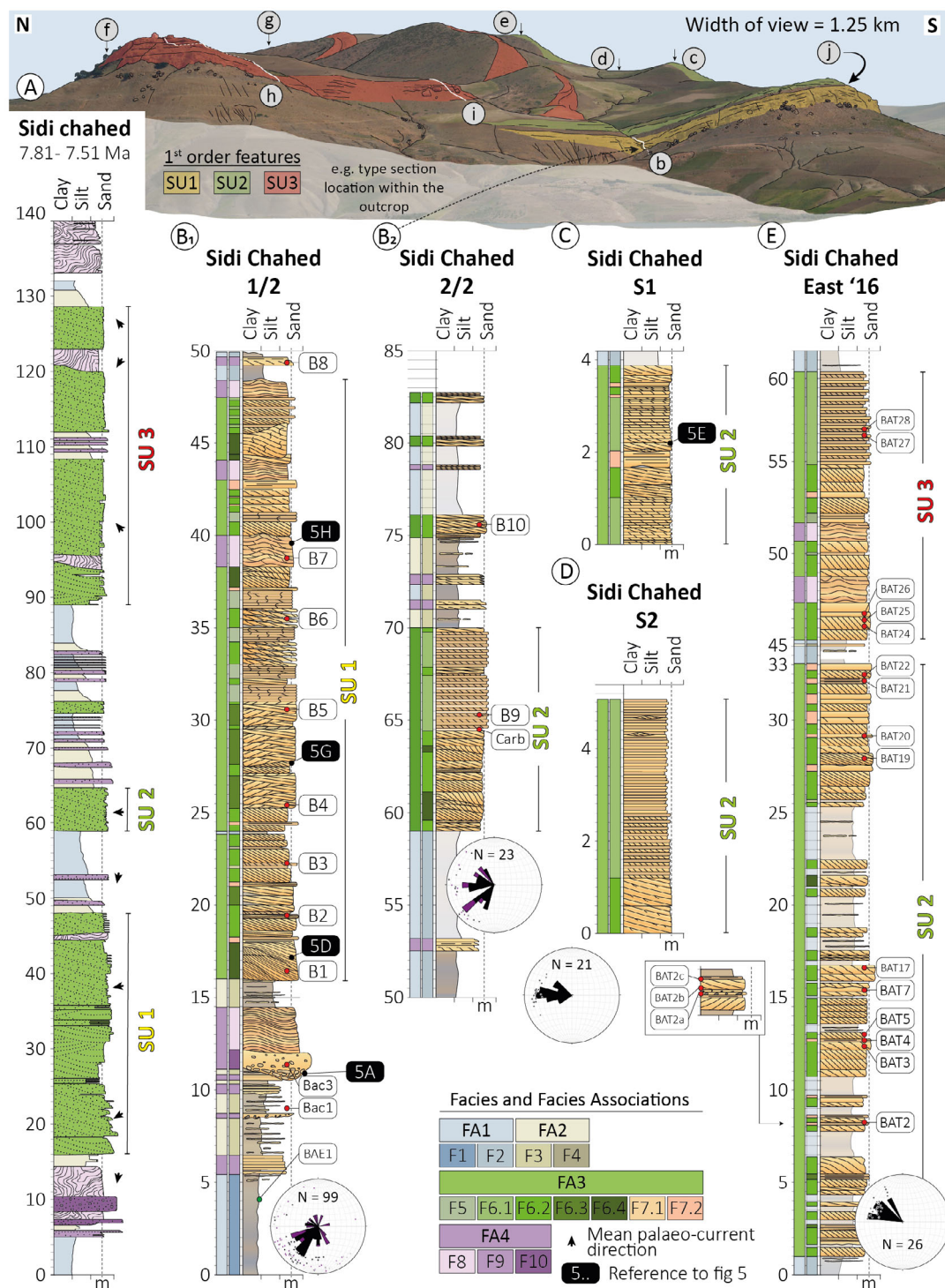
Fig. 3. (Above) Overview figure of the Sidi Chahed outcrop (A) and associated sections (B) to (E). The log on the left represents a generalized composite log through the three main first-order sand units (SU), the black arrows indicate mean palaeocurrent directions with respect to the north (up). (A) Panoramic picture of the outcrop. In yellow, green and red, respectively, the palaeochannels SU1, SU2 and SU3. The small grey circles with small letters depict the location of the sections (B) to (I) and the location of (J). The black, numbered, text balloons show the location of the pictures in Fig. 5. (Right) Sections (F) to (I) of the Sidi Chahed outcrop. (J) Drawing of the south-western flank of the outcrops as indicated in (A). This sketch shows the first-order lower-bounding surfaces (LBS) and upper-bounding surfaces (UBS) as well as the second-order bounding surfaces.
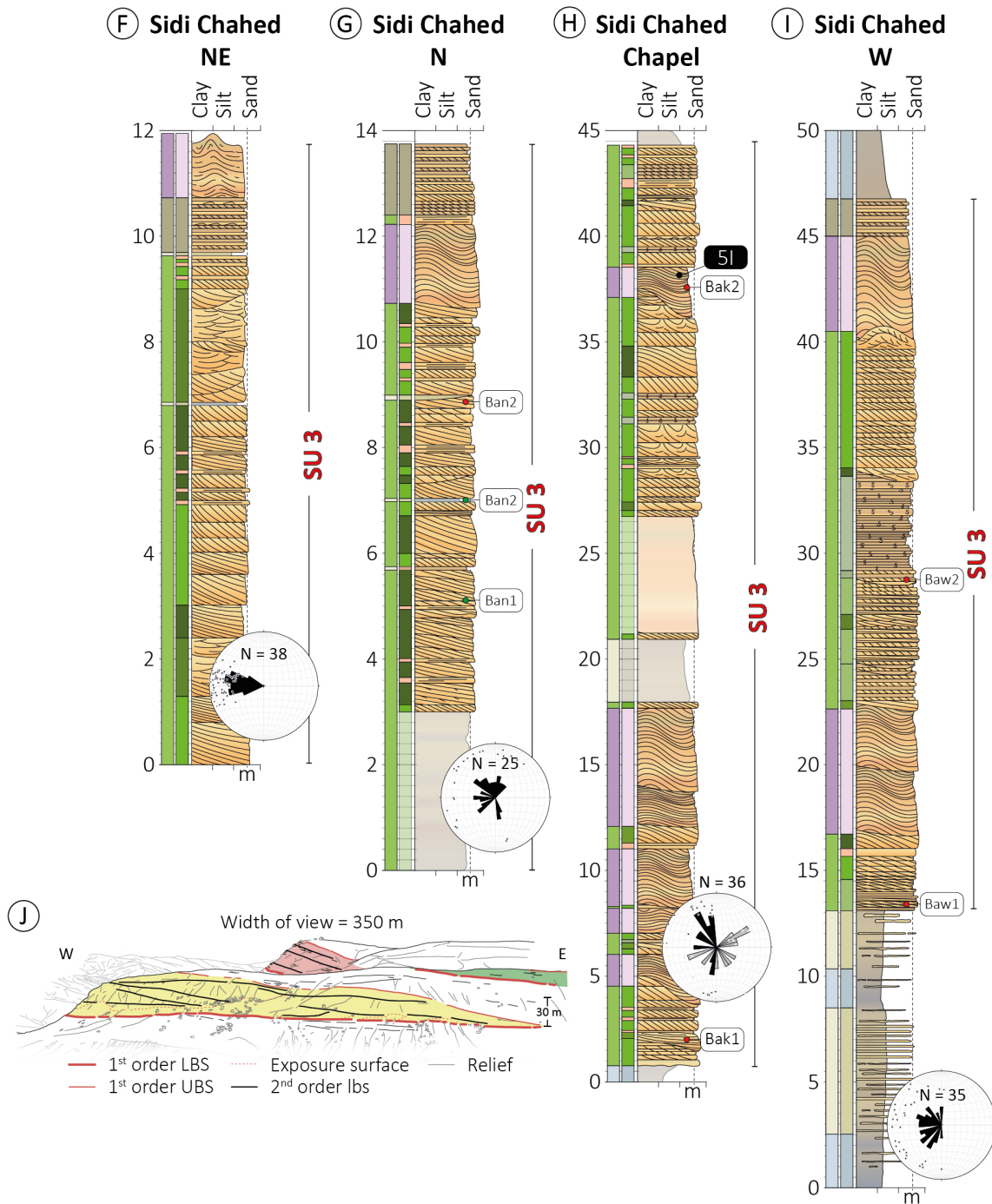
Fig. 3. (Continued)

water and deep-water species. The species *Planulina ariminensis*, *Sphaeroidina bulloides*, *Uvigerina semiornata* and *Uvigerina peregrina* are present throughout (including samples obtained from marlstone interbedded within the sandstone units), and *Cibicidoides kullenbergi* occurs

in about half of the samples, indicating upper bathyal environments roughly equivalent to the upper slope physiographic domain (250 to 400 m water depth). The upper part of the section contains lesser slope taxa, indicating a slightly shallower depth range (upper slope–
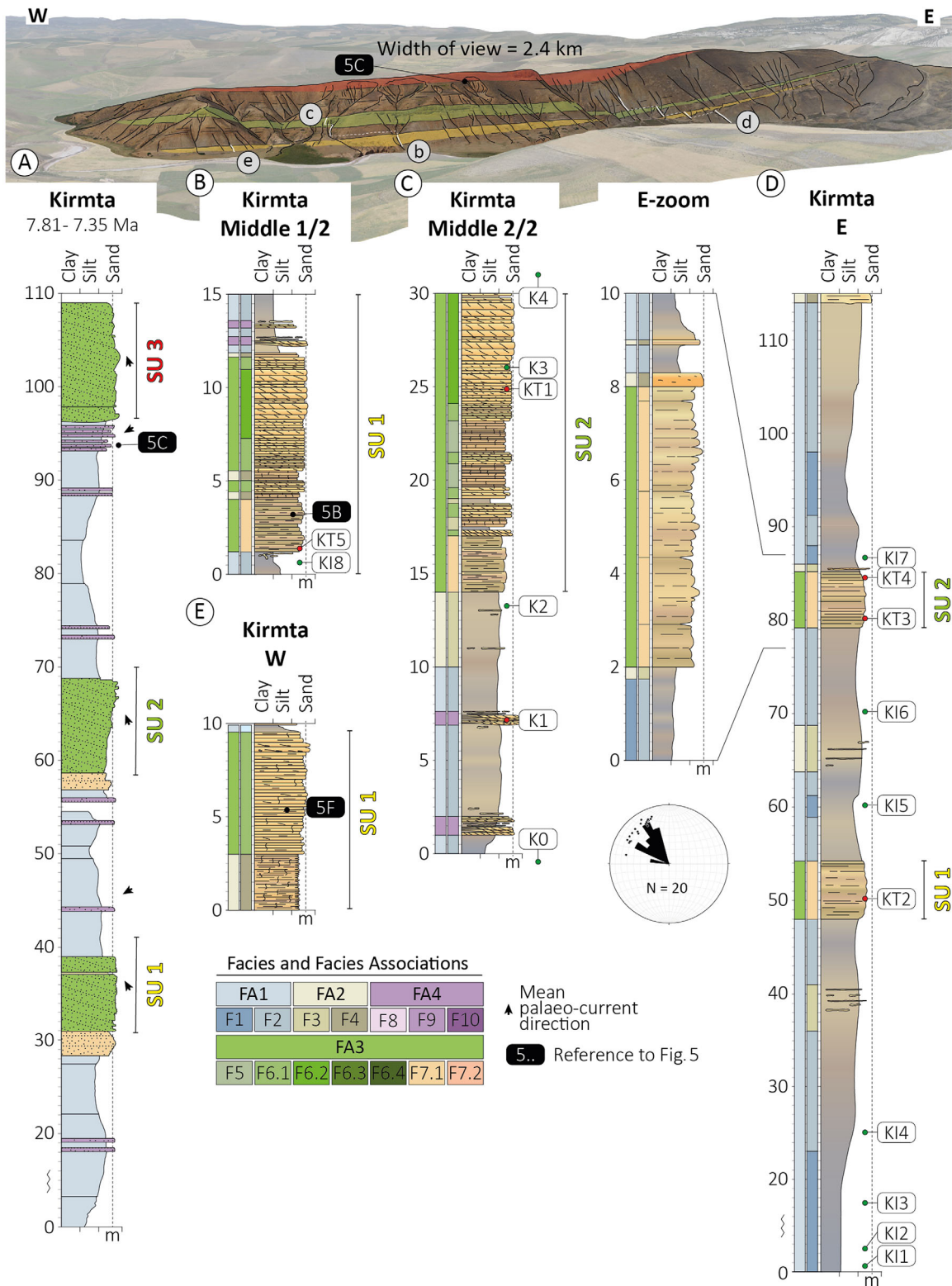
Fig. 4. Overview figure of the Kirmta outcrop (A) and associated sections (B) to (E). The log on the left represents a generalized log through the three first-order sand units, the black arrows indicate the mean palaeocurrent directions with respect to the north (up). (A) Panoramic picture of the outcrop photographed towards the north. In yellow, green and red, respectively, the palaeochannels SU1, SU2 and SU3. The small grey circles depict the location of the sections. The black, numbered, text balloons show the location of the pictures in Fig. 5.

outer shelf physiographic domain, 150 to 300 m water depth) (Capella *et al.*, 2017; Tulbure *et al.*, 2017).

The Kirmta section, based on the foraminiferal assemblage of 12 samples has been assigned to the *Globigerinoides obliquus extremus/Globorotalia suterae* biozone MMi-12b of Lirer *et al.* (2019). The marls contain abundant planktonic and benthic foraminifera, but the proportion of benthic foraminifera is always lower (20 to 40%). Based on the common occurrence of *Globorotalia merardii 4*, whose last common occurrence was at 7.51 Ma (Sierro, 1985; Sierro *et al.*, 1993, 2001; Hilgen *et al.*, 2000; Capella *et al.*, 2017) and the presence of *Globorotalia suterae* whose first occurrence has been proven at 7.8 Ma (Lirer *et al.*, 2019), the section was dated between 7.8 Ma and 7.51 Ma. In all samples the assemblages of planktonic foraminifera are similar, showing scarce keeled Globoratalids, more abundant *Globorotalia scitula* (sinistral and dextral) and abundant *Globigerinoides extremus*, *Globigerina bulloides*, Neogloboquadrinids (mainly sinistral) and in some samples common *Dentoglobigerina altispira*.

The benthic foraminifer assemblages of the samples contain rare shallow-water species: *Ammonia*, *Nonion* and more frequent deep-water species: *Uvigerina peregrina*, *Uvigerina semiornata*, *Pullenia bulloides*, *Martinottiella communis*, *Cibicidoides pachyderma*, *Sphaeroidina bulloides*, *Marginulina costata*, *Buliminids*, *Trifarina*, *Gyroidina*, *Lenticulina*, *etc*. Based on these assemblages and the high percentages of planktonic foraminifera in most of the samples, it is inferred that the water depth of the physiographic domain where the sediments were deposited was equivalent to the outer shelf and/or upper slope (150 to 300 m water depth) (Capella *et al.*, 2017; Tulbure *et al.*, 2017), with the common presence of shallow benthic foraminifera living in the shelf that were probably transported down-slope through the shelf–slope break.

Sedimentary facies description

Ten different sedimentary facies (F1 to F10) have been distinguished within the fine-grained deposits (marls) and the sandstone units (channels) in the two studied sections (Table 1, Fig. 5). The sedimentary facies include: F1, fossil-rich blue marlstone; F2, sandy marlstone; F3, sandstone laminae; F4, heterolithic sandstone; F5, fully-bioturbated sandstone; F6, cross-stratified sandstone; F7, planar-laminated sandstone; F8, convolute sandstone; F9, amalgamated normal-graded sandstone; and F10, conglomerate.

F1 – Fossil-rich blue marlstone
Facies F1 consists of blueish marls – the sediments after which the Blue Marl Formation is named (Table 1, Fig. 5A and B). These mainly structureless, fossil-rich marlstones (containing bivalves up to centimetre-scale) occur as laminae interbedded with sandstone or continuous sequences of up to hundreds of metres in thickness. Despite being dominantly blueish in colour, gradational changes from dark blueish grey to more brownish grey are common. This colour change results from slight increases in the siliciclastic fraction consisting of up to very fine-grained sand. F1 shows only scarce discrete trace fossils.

F2 – Sandy marlstone
Facies F2 consists of fossil-rich sandy marlstones and very fine-grained muddy sandstones (Table 1, Fig. 5A and C). This facies regularly occurs in gradational alternation with the fossil-rich blue marlstone (F1) consisting of continuous sequences of up to metre-scale thickness. The texture is homogeneous for the finest intervals that are more blueish grey in colour (similar to F1). The coarser and more light-brownish grey intervals are regularly banded or laminated. Changes in grain-size distribution are generally gradational, but sharp basal contacts have been observed between more muddy and more sandy deposits. Starved ripples of fine-grained sand are scarce. Laminae with sharp basal bounding surfaces and ripples coincide with an increased abundance of fine-grained shell fragments whereas the muddier intervals regularly contain well-preserved bivalves up to 1.5 cm in diameter. The trace fossil assemblage consists of abundant undifferentiated structures and scarce *Planolites*-like and *Thalassinoides*-like traces.

F3 – Sandstone laminae
Facies F3 consists of discontinuous slightly undulatory, lenticular, up to fine-grained sand laminae that only rarely exceed 1 cm in thickness (Table 1, Fig. 5A and D). The sand consists of a mixed siliciclastic–bioclastic composition; encased within facies F2. These laminae and sand lenses occur over short (up to 1 m) intervals where the sand (facies F3)/silt (facies F2) ratio is approximately 1:4. The trace fossil assemblage consists of abundant undifferentiated

structures and scarce *Planolites*-like and *Thalassinoides*-like traces.

F4 – Heterolithic sandstone

Facies F4 typically consists of heterolithic, tabular, dominantly very thin to thin bedded (<5 cm), compositionally mixed (bioclastic dominated), up to fine-grained sandstone and siltstone with an average ratio of 3:1 (Table 1, Fig. 5E and F). The sandstone hosts remnants of dominantly unidirectional, along-slope oriented cross-lamination. The trace fossil assemblage consists of abundant undifferentiated structures and scarce *Macaronichnus*, *Planolites*-like and *Thalassinoides*-like traces.

F5 – Fully bioturbated sandstone

Facies F5, consisting of coarse-grained mixed compositional siliciclastic–bioclastic sand is fully reworked by *Macaronichnus* ichnofacies (Fig. 5F). The sandstone, dark brown in colour, shows remnants of tabular bedding (10 and 15 cm) and occasional signs of parallel lamination (Table 1, Fig. 5F and G). Besides being dominated by *Macaronichnus*, the trace fossil assemblage consists of scarce *Scolicia*, *Planolites* and *Thalassinoides*-like traces.

F6 – Cross-stratified sandstone

Facies F6 consists of compositionally mixed, siliciclastic–bioclastic, unidirectionally cross-stratified sandstones (Table 1, Fig. 5). Due to the occurrence of a variety of sedimentological characteristics this facies has been divided into four sub-facies: (i) (F6.1) thin-bedded cross-stratified sandstone (Fig. 5B and F); (ii) (F6.2) medium to thick-bedded cross-stratified sandstone (Fig. 5B, D and G); (iii) (F6.3) trough cross-stratified sandstone (Fig. 5G); and (iv) (F6.4) tangentially cross-stratified sandstone (Fig. 5D). This facies commonly shows a pale/dark centimetre-scale banding within foresets (Fig. 5). The paler bands are dominated by bivalve fragments up to several millimetres long, together with a variety of other bioclast types, and are cemented by sparry calcite (Table 1, Fig. 6). The darker bands also contain bioclasts, but they are smaller (sand-grained) in size. Furthermore, these bands contain numerous rounded pellets of dark claystone, usually contain brownish glauconite and are cemented by sparry calcite, albeit less prominently, as porosity is lower. The trace fossil assemblage consists of abundant *Scolicia* and *Macaronichnus*, and rare *Planolites* and *Thalassinoides* with common undifferentiated horizontal biogenic structures.

F6.1 – Thin-bedded sandstone. Sub-facies F6.1 consists of tabular, medium-grained sandstone beds with unidirectional top-cut cross-strata (Table 1, Fig. 5B and F). Bed thicknesses range from 5 to 15 cm. Due to weathering; it is apparent that this facies regularly is interbedded with more easily erodible sediment forming alterations between cemented and unconsolidated beds. These alterations are related to foreset banding as described above, where the finer-grained, darker band of each foreset was more prone to erosion.

F6.2 – Medium to thick-bedded sandstone. Sub-facies F6.2 consists of tabular, medium-bedded to thick-bedded (15 to 100 cm), moderately-sorted to well-sorted, up to coarse-grained sandstone with unidirectional cross-strata (Table 1). The cross-strata regularly reflect bundles of thickening and thinning foresets that show modest alternations between angular to tangential toe-set geometries (Fig. 5D and E). Toe-sets are commonly enriched in bioclastic material. Basal boundaries are sharp (for example, Fig. 5E) and occasionally contain muddy rip-up clasts. Soft sediment deformation structures are most common in this sub-facies, regularly being present as overturned folds (Fig. 5G) and fluid escape structures (Fig. 5H and I).
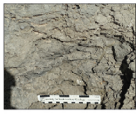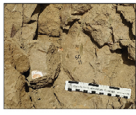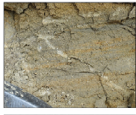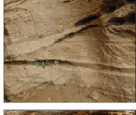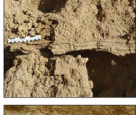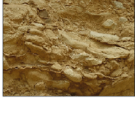
F6.3 – Trough cross-stratified sandstone. Sub-facies F6.3 is typified by trough cross-stratified, medium-grained, sandstone (Table 1, Fig. 5G). Foresets are convex-up and alternate between more orange and darker brownish colours that reflect changes in the abundance of bioclastic material. The concave-up bedform geometries are typically between 5 to 10 m wide and up to a metre in thickness.

F6.4 – Tangential cross-bedded sandstone. Sub-facies F6.4 consists of very thick (*ca* 2 m), cross-stratified, up to coarse-grained sandstones with toe-set geometries that cyclically change from tangential to angular (Table 1, Fig. 5D). Toe-sets are enriched in bioclastic material and show a higher intensity of bioturbation. Internally, erosional sigmoidal bounding surfaces are common.

F7 – Planar-laminated sandstone

Facies F7 is typified by the presence of planar-laminated, tabular beds of compositionally mixed siliciclastic–bioclastic, up to coarse-grained sandstone (Table 1). Since the lithology varies

Table 1. Sedimentary facies and facies associations table including the colour codes used throughout the chapter, sedimentary structures, thickness, grain-size, percentage of bioclastic component (Bc%), biogenic structures, estimated current velocities in $\mathrm{cm\,s^{-1}}$ ($\mathrm{v\,cm\,s^{-1}}$) and microfacies (MF).

FA	Picture	Sed. facies	Sed. structures	Thickness	Grain-size	Bc%	Bioturbation	v cm s⁻¹	MF
FA1. Hemipelagic/Drift		F1. Fossil-rich blue marlstone	Massive to gradational	Up to 1 km	Clay, silt & very-fine sand < 0.125 mm		Scarce discrete trace fossils	< 5	–
		F2. Sandy marlstone	Massive, gradational or sharp basal surfaces	Up to 10's of metres	Clay, silt & fine sand < 0.25 mm		Ab. undiff. scarce *Planolites*- and *Thalassinoides*-like	5 to 15	–
FA2. Transitional		F3. Sandstone laminae	Lenticular laminae	< 1.5 cm	Fine sand 0.125 to 0.25 mm		Scarce *Planolites*- and *Thalassinoides*-like	10 to 20	–
		F4. Heterolithic sandstone	Tabular bedding with remnants of ripples	1 to 5 cm	Sand & marl < 0.5 mm		Ab. undiff. *Macaronichnus Planolites*- and *Thalassinoides*-like	10 to 40	I
FA3. Contourite channel		F5. Fully bioturb. sandstone	Remnants of parallel lamination	10 to 15 cm	Coarse sand 0.5 to 1.2 mm		*Macaronichnus*, scarce *Scolicia*, *Planolites* and *Thalassinoides*-like	35 to 50	III
		F6. Cross-strat. sandstone (2D-dunes)	F6.1 Thin-bedded	5 to 15 cm	Medium sand 0.25 to 0.5 mm		Abundant *Macaronichnus* and *Scolicia*, common undif. hor. biogenic structures, rare *Planolites* and *Thalassinoides*-like	40 to 60	II to III
			F6.2 Medium- to thick-bedded	0.1 to 1 m	Medium sand 0.25 to 0.5 mm			40 to 60	II to III
		F6. Cross-strat. sandstone (3D-dunes)	F6.3 Trough cross-bedded	0.5 to 1 m	Medium sand 0.25 to 0.5 mm			60 to 100	II to III
			F6.4 Tangentially cross-bedded	~ 2 m	Medium sand 0.25 to 0.5 mm			80 to 120	I to II
		F7. Planar lam. sandstone	F7.1 Bi-gradational silty sandst.	5 to 20 cm	very fine to fine sand 0.062 to 0.25 mm		Abundant undiff. biogenic structures, scarce *Macaronichnus*, *Planolites* and *Thalassinoides*-like	60 to 100	I
			F7.2 Planar laminated sandst.	10 to 40 cm	Medium sand 0.25 to 0.6 mm			100 to 180	III
FA4. Gravitational		F8. Convolute sandstone	Convolute, contorted and soft-sediment deformation	Up to 3 m	Sand < 0.6 mm		Difficult to appreciate		II to III
		F9. Amalgamated normal graded sandstone	Massive, planar laminae, ripples and basal scours	< 40 cm	Sand to silt occasional up to pebble sized rip-up clasts		Scarce undiff., occasional *Planolites*		II to III
		F10. Conglomerate	Monomictic, deeply incised lower bounding surface	< 3 m	Up to cobble sized clasts in arenitic matrix		None		–

between fine-grained and coarse-grained sand this facies has been divided into two sub-facies (F7.1 and F7.2, Fig. 5B and D, respectively). The trace fossil assemblage consists of abundant undifferentiated structures and scarce *Macaronichnus*, *Planolites*-like and *Thalassinoides*-like traces.

F7.1 – Bi-gradational silty sandstone. Sub-facies F7.1 has only been recognized in the Kirmta outcrop and consists of stacked, tabular, planar parallel laminated, successively inverse-graded then normally-graded (bi-gradational) sandstone beds with thicknesses ranging from 5 to 20 cm (Table 1, Fig. 5B). A bi-gradational pattern has also been observed on a bed-set scale (0.5 to 1.2 m). This facies typically consists of very fine-grained to fine-grained sand of dominantly siliciclastic composition. Furthermore, it is rich in sand-sized pellets of mudstone and brownish glauconite.

F7.2 – Planar-laminated sandstone. Sub-facies F7.2 consists of tabular, planar-laminated sandstone beds that range in thickness between 10 and 40 cm (Fig. 5D). The sandstone beds generally consist of coarse-grained sand and the abundance of bioclastic material determines the differentiation between laminae. This facies generally lacks or shows a very low abundance of trace fossils.

F8 – Convolute sandstone

Facies F8 consists of thin bedded (up to 10 cm) convolute strata. Fluid escape structures are common in the underlying sandstone (Table 1, Fig. 5H and I). The primary beds were either cross-stratified sandstones (F6) or amalgamated, normal graded sandstones (F9). The lower bed bounding surface is sharp and erosive (Fig. 5H). This facies appears wedge shaped, thinning out perpendicular to the dominant dip direction of cross-beds in facies F6, in an inferred up-slope direction. Inclination of the preserved primary strata varies laterally from high-angle to opposing angles (−20°) down-dip with respect to the inferred palaeo-slope. Trace fossils are difficult to identify.

F9 – Amalgamated, normal-graded sandstone

Facies F9 consists of dominantly tabular, hetero-lithic, normal graded, amalgamated sandstone and mudstone with bed thicknesses averaging 5 to 10 cm, never exceeding 40 cm (Table 1, Fig. 5C). Although a semi-gradational transition from sand to mud occurs, boundaries can be easily distinguished. This facies regularly shows plane-parallel lamination and ripples and is capped by a very thin siltstone grading to marl-stone. Basal scours and marly rip-up clasts are common. The well-sorted to very well-sorted, up to medium-grained sand predominantly consists of siliciclastic material but has a bioclastic component. This facies is bioturbated with scarce undifferentiated discrete trace fossils, and only occasional *Planolites* can be recognized.

F10 – Matrix-supported conglomerate

This monomictic conglomerate changes upward from an ortho-conglomerate to para-conglomerate (Fig. 5A). The clasts are poorly sorted, rounded and disc shaped, dominantly consisting of arenitic cobbles and boulders. The matrix consists of silty sand and the basal bounding surface is deeply incised in the underlying sandy marls belonging to facies F3. No biogenic structures were observed.

Petrographic analysis

The petrographic samples examined are derived from indurated sandstones related to facies F4, F6, F7, F8 and F9 (Table 1; Figs 3 and 4). All samples contain the same range of detrital components, but their proportions and rock fabric vary. Examples based on modal analysis of five samples are provided in Table 2. The detrital components include bioclasts, of which bivalve fragments are usually most common, together with fragments of echinoids, benthic and planktonic foraminifera, calcareous algae, occasional bryozoa and other unidentified bioclasts. Bivalves and other elongate fragments are often aligned horizontally to the bedding (for example, Fig. 6A and B). Many of the bioclasts are fragmented and display signs of transport. Individual bioclasts typically occur as sand-grade fragments, and their small size and common recrystallization often impedes their identification. The bioclasts within the coarsest-grained samples seldom exceed 5 mm in size. Rounded sand-sized grains of limestone, usually comprising variably recrystallized calcite, are common, and large dolomite rhombs which often display signs of erosion and transport also occur (Fig. 6C).

Quartz grains, typically sub-rounded with a grain size of fine-grained to medium-grained sand, are almost always present, but usually form a subordinate component of the sample. Pellets of glauconite are also recognized in
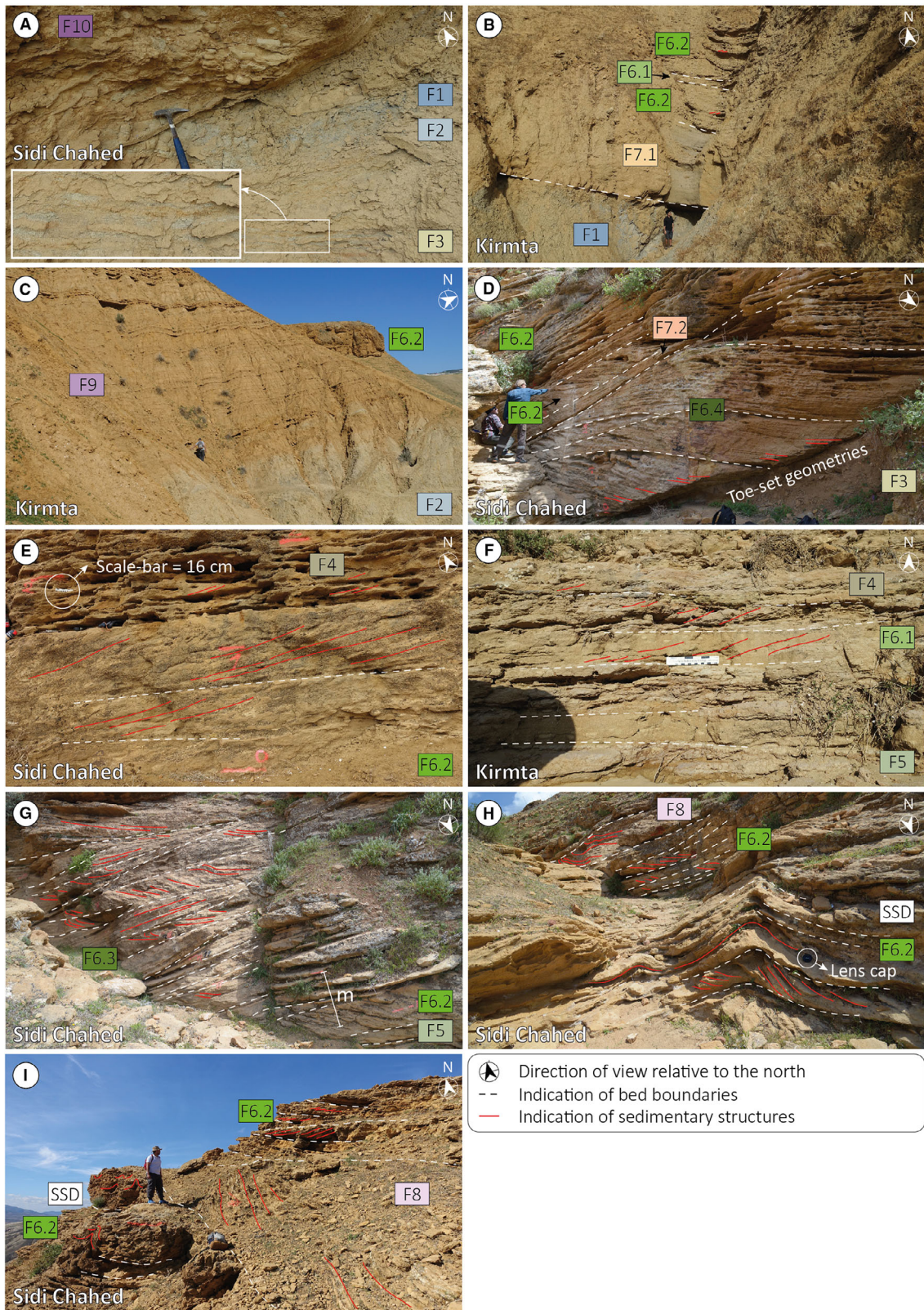
Fig. 5. Outcrop pictures associated with the studied channelized features with facies labels. (A), (D), (E), (G), (H) and (I) are from the Sidi Chahed outcrop. (B), (C) and (F) are from the Kirmta outcrop. SSD, soft sediment deformation. The people representative for scale are between 1.7 m and 1.95 m.

© 2022 The Authors. *Sedimentology* published by John Wiley & Sons Ltd on behalf of International Association of Sedimentologists., *Sedimentology*, **70**, 611–644

PPL   XPL
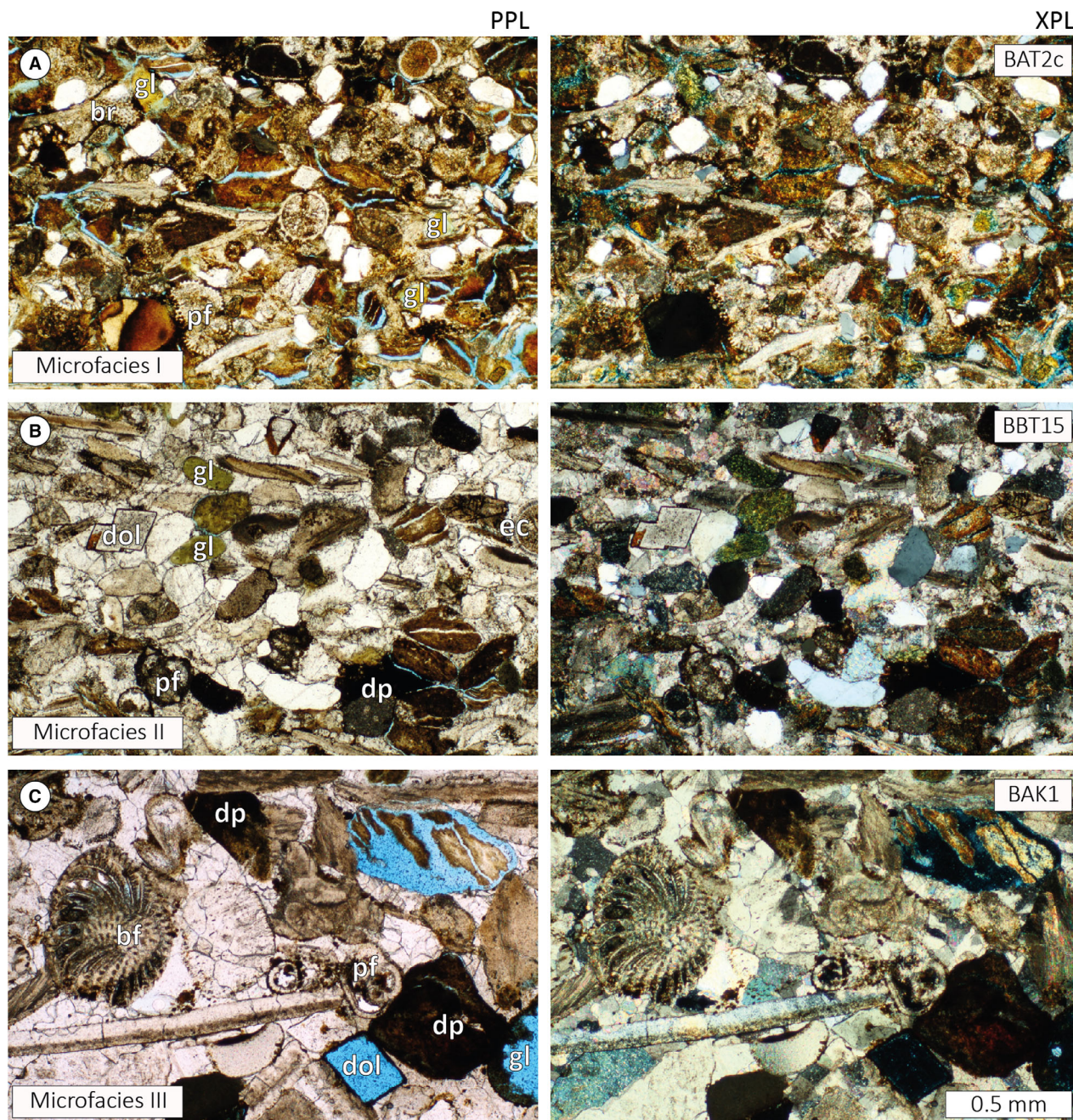
Fig. 6. Thin-section images of the three microfacies identified: (A) Microfacies 1; (B) Microfacies 2; and (C) Microfacies 3. The pictures on the left-hand side are in plane-polarized light whereas the pictures on the right-hand side are in cross-polarized light. The scale of the pictures is provided in the lower left corner. Abbreviations in the pictures stand for: gl, glauconite; br, bryozoan fragments; ec, echinoderm fragments; pf, planktonic foraminifera; bf, benthic foraminifera; dp, detrital pellets; commonly consisting of mud; and dol, dolomite.

almost all samples (Fig. 6), usually brown or olive-yellow and reworked, but fresher green pellets have also been observed. Feldspar grains and mica flakes occur in small proportions.

Heavy minerals are uncommon – several grains of tourmaline, rutile and possible small zircons have been observed. There is sometimes a brown argillaceous matrix, commonly silty, which

Table 2. Modal analysis data based on 300-point modal analysis in thin section.

Sample	MF	Qm	Qp	Qt	F	Gg	Gb	Gt	Lc	Ld	Lcp	Lfa	Lqm	Lt
BAT2a	II	7.2	0.0	**7.2**	0.0	0.0	2.1	**2.1**	12.0	0.0	14.0	0.0	0.0	**26.0**
BAT2b	I–II	14.3	0.7	**15.0**	0.3	Tr	5.9	**5.9**	11.8	0.3	16.0	0.7	0.0	**28.8**
BAT2c	I	12.2	2.2	**14.4**	0.4	0.0	3.6	**3.6**	14.7	0.7	24.7	0.0	0.4	**40.5**
BAT4	II	9.7	1.8	**11.5**	0.9	0.0	3.1	**3.1**	18.1	0.0	11.9	0.0	0.0	**30.0**
BAT14	II	12.0	2.1	**14.1**	0.0	0.0	7.9	**7.9**	14.9	0.0	4.6	0.0	0.0	**19.5**

Sample	Bb	Bf	Be	Bca	Bu	Bt	Cc	Fe	P%	GS	S
BAT2a	20.9	2.7	1.0	Tr	14.1	**38.7**	25.3	0.7	2.7	Fs	w
BAT2b	12.9	2.8	0.3	1.3	21.7	**39**	10.1	0.7	4.3	Fs	w
BAT2c	5.4	5.0	0.0	0.0	20.8	**31.2**	9.3	0.4	7.0	Fs	w
BAT4	21.4	1.8	0.0	2.0	16.1	**41.3**	11.9	1.3	24.3	Ms	w-vw
BAT14	15.4	2.5	0.7	1.3	20.0	**39.9**	17.8	0.8	19.7	Ms	w-vw

Proportions of solid rock components (all but porosity) are renormalised to a total of 100%. Component abbreviations, from left to right: MF, microfacies; Qm, Monocrystalline Quartz; Qp, Polycrystalline Quartz; Qt, Quartz total; F, Feldspar; Gg, Green glauconite; Gb, Brownish/yellowish glauconite; Gt, Glauconite total; L, Lithic fragments; c, carbonate; d, dolomite; cp, claystone pellets; fa, feldspar aggregates; qm, quartz–mica aggregates; Lt, Lithic total; B, Bioclastic; b, bivalves; f, foraminifera; e, echinoderm; ca, calcareous algae; u, undifferentiated; Bt, Bioclast total; Cc, Calcite cement; Fe, Iron Oxides/Hydroxides; P%, porosity percentage; GS, Mean grain size (ms, medium-grained sand, fs, fine grained sand); S, Sorting (w, well, vw, very well). Bold values represent the total of particular components. E.g. Monocrystalline quartz (Qm = 7.2%) + Polycrystalline quartz (Qp = 0%) (Qt in bold) is the total percentage of the component quartz = Qm + Qp = Qt.

may be patchily distributed or form thin irregular laminae which may be deformed. A pervasive argillaceous matrix is uncommon. Sand-sized pellets of brown claystone are common, some apparently partially glauconitized. Most samples are cemented by sparry calcite, or sometimes a more finely crystalline calcite, although the cement (together with other carbonate components of a sample) has often suffered dissolution.

Three main 'microfacies' have been defined, forming a spectrum along which almost all of the samples examined can be placed. Microfacies I (MF1) (Fig. 6A) is relatively fine-grained and contains abundant argillaceous components such as clay pellets and glauconite. Microfacies III (MF3) (Fig. 6C) is a relatively coarse bioclastic limestone. Microfacies II (MF2) (Fig. 6B) is intermediate in composition and grain size. In most cases the boundary between one microfacies and another observed in thin section is gradational. Both fining-up and coarsening-up trends are observed in thin section.

Overall, most samples of facies F4 and F7.1 belong to MF1. Most samples of facies F6 are transitional between MF1 and MF3, and most samples of facies F5 and F7.2 are MF3. The samples of the Kirmta sections, on average, are finer grained compared to the samples of the Sidi Chahed sections,

with half of the samples being assigned to MF1 and the other half dominantly consisting of MF2.

Facies associations and interpretations

The sedimentary facies are grouped, primarily based on spatial co-occurrences and gradational contacts as well as grain size, to form four distinct facies associations and depositional elements (Table 1). The finest-grained sediments are grouped into facies association 1 and consist of both fossil-rich blue marls (F1) and sandy marl-stones (F2) which regularly grade into one another. Facies association 1 (FA1) occurs over intervals upward of tens to hundreds of metres in thickness. FA1 is generally coarsening-upward, grading from F1 to F2 towards the base of the sand units (Figs 3 and 4). Facies association 2 (FA2), consisting of sandstone laminae (F3) and heterolithic sandstone (F4), contains transitional facies between FA1 and FA3. This facies association is marked by the presence of co-occurring heterolithic sand and fine-grained sediment unlike FA1. In facies association 3 (FA3), occurring within the channels, all facies (from F5 to F7) are found interbedded with one another. However, they generally grade both upward and laterally with the facies from planar laminated sandstone (F7) to cross-stratified sandstone (F6) and fully

bioturbated sandstone (F5). Facies association 4 (FA4), consisting of convolute sandstone (F8), amalgamated normal graded sandstone (F9) and conglomerates (F10), is typified by the presence of sedimentary structures that are directed parallel to the inferred palaeo-slope and perpendicular to those observed in FA3. The convolute sandstones (F9) are regularly found interbedded within FA3, occurring within the channels. Facies F9 is always found in association and amalgamated with facies association 1 (Figs 3 and 4) and is only recognized outside the channels. Conglomerates (F10) are only present at one location in the Sidi Chahed section, interbedded between F3 and F8 (Fig. 3B).

Fine-grained marine sediment (FA1)
The fine-grained sediment of FA1, the blue marls (Table 1), are the same as previously described in de Weger *et al.* (2020, 2021). Since the facies (F1 and F2) of this facies association are not the focal point of this work and they are similar to FA1 as previously described in de Weger *et al.* (2020, 2021), these authors' interpretation is directly applied. Facies association 1 is thus interpreted to represent a low energy depositional environment dominated by the vertical settling and lateral advection of both fine-grained biogenic and terrigenous particles (hemipelagic sedimentation) and the activity of weak bottom currents resulting in drift deposits. Furthermore, there was a likely presence of occasional low-density turbidity currents (F2).

Contourite channel-drift transition (FA2)
Within FA2, the sandstone laminae (F3) represent the lowest energy conditions. Because F3 is closely associated with FA2, its origin is also likely related to bottom current processes. As such, the lenticular sand laminae of facies F3 represent starved ripples formed by high energy flow-conditions in an environment otherwise dominated by suspension fallout related to weaker current velocities. This indicates that flow conditions alternated between low to moderate current strengths with associated periods of winnowing (Martín-Chivelet *et al.*, 2008). Similar facies were also recognized in the Gulf of Cadiz by de Castro *et al.* (2020, 2021) and in similar but different outcrops in Morocco by de Weger *et al.* (2021) who interpreted these deposits as bottom current reworked sands formed by moderate but intermittent bottom currents capable of reworking gravity driven flow deposits which supplied sediment to the system. This

facies is ascribed to a channel-drift transition environment, marked by stronger/weaker current activity compared to the drift/channel (Fig. 7).

The heterolithic sandstones (F4) are more closely related to FA3 compared to FA1, where facies F4 often represents the lateral equivalent of the larger cross-stratified bedforms of F6.1 and F6.2. In comparison to F3, the cross-laminated sandstone beds are better developed, and the sand/mud ratio is higher, indicating higher mean-current velocities and a possible increase in sediment supply. With respect to the findings of de Weger *et al.* (2021), this facies is intermediate to F4 (heterolithic sandstone and mudstone) and F5 (cross-stratified and rippled sandstone) described therein (Fig. 7), allowing for an assignation in the channel-drift transitional domain. The heterolithic nature of the beds suggests alternating flow conditions between bedload transport and suspension fallout. These alterations might have been induced by the tidal modulation of the palaeo-MOW (de Weger *et al.*, 2021) or have resulted from other, longer timescale control on overflow behaviour responsible for the expanse and collapse of the bottom-current core.

The undifferentiated biogenic structures together with *Macaronichnus* and *Planolites*-like burrows indicated that benthic food was concentrated on the seafloor and within the upper centimetres of the substrate. The higher abundance and diversity of trace fossils in facies F4 with respect to F3 can be related to the increased availability of benthic food, which in turn is likely associated with an increase in sediment supply.

Contourite channel (FA3)
The commonality of the facies ascribed to facies association 3 (Table 1) is that they show traction structures in the form of planar-directional and unidirectional cross-stratification (F5, F6 and F7). This facies association occurs over thick intervals (generally over 5 m in thickness) where related facies occur both stacked and in lateral transition. Only minor intervals (facies F3 and F4) indicative of weaker current velocities are present (Figs 3 and 4). These characteristics indicate that flow conditions were relatively persistent with high flow velocities. The alternation of sedimentary facies and the presence of erosive surfaces, however, suggest that current velocities fluctuated but, in general, remained high enough to erode and redistribute medium-grained to coarse-grained sand. The erosive (or
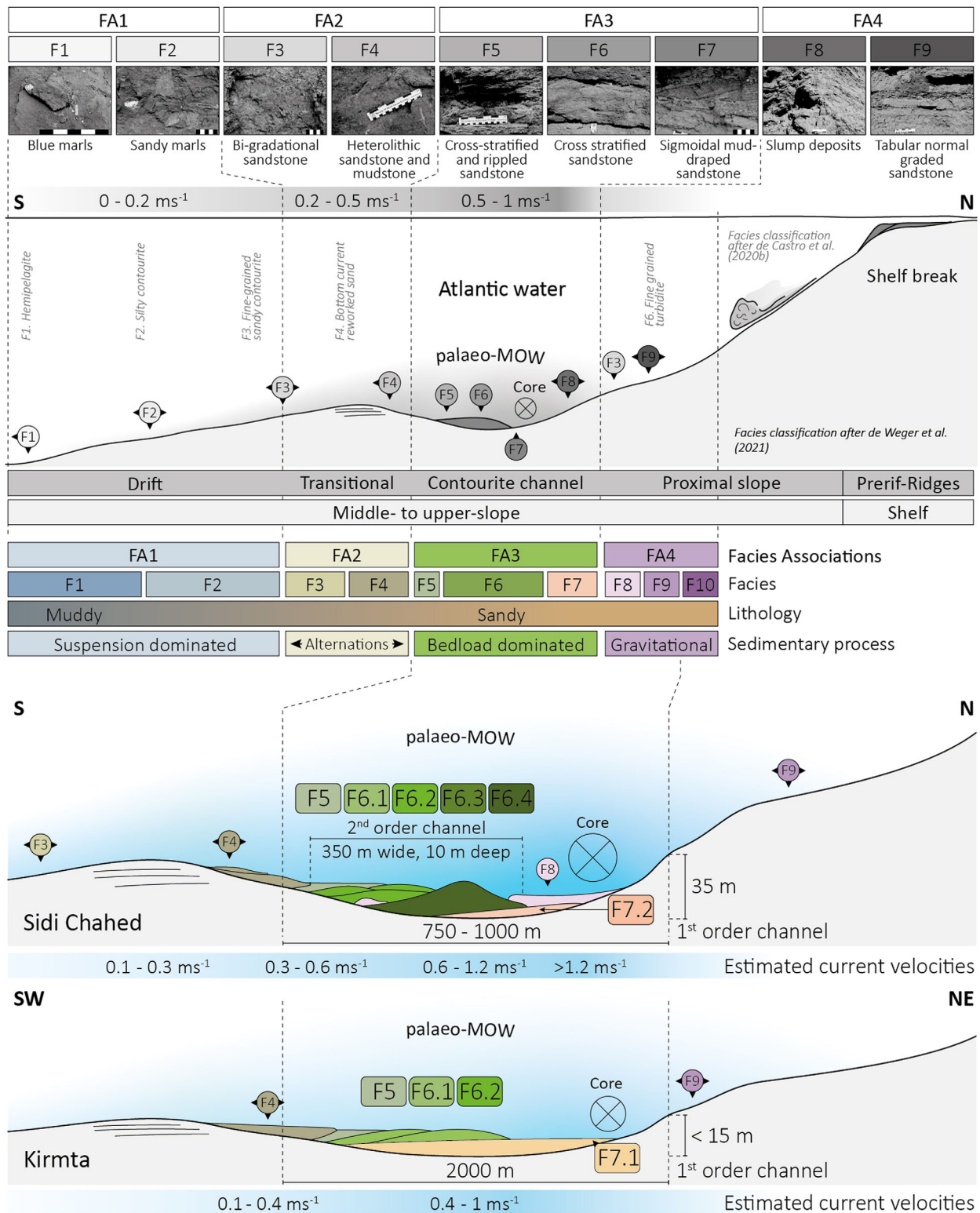
Fig. 7. The top panel is derived from de Weger *et al.* (2021) and shows the relation between facies F1 to F9 defined therein. This facies model is used for comparison to the newly proposed facies model made herein (two bottom panels, one for the Sidi Chahed and one for the Kirmta outcrop). This facies model shows the relation between facies and facies associations within the first-order contourite channel, which transitions towards the drift (south/south-west or left). The estimated current velocity for each depositional domain is included.

reactivation) surfaces could also indicate periods of decreased sediment supply as well as the intermittent behaviour of the bottom current through time. The presence of tidal signatures, such as thickening and thinning foreset-bundles (Allen, 1982; Longhitano & Nemec, 2005), gradual changes between angular to tangential toe-set geometries (*sensu* Chiarella, 2016), and foreset composition couplets (Ichaso & Dalrymple, 2009; Longhitano *et al.*, 2012) indicate that deposition took place in a tidally-influenced environment. This suggests that the formation of the cross-stratified beds took several tidal cycles (months to years), ruling out a turbiditic origin of these deposits. De Weger *et al.* (2021) argued that these tidal signatures in deep-water environments of the Rifian Corridor resulted from tidal modulation of the palaeo-MOW, most prominently observed within contourite channel deposits. This, combined with the strong energy conditions required for the deposition of these sediments, allows the assignation of this facies association to the contourite channel (Fig. 7). The general scarcity of trace fossils is consistent with persistent high energy conditions hindering bioturbation by trace makers.

Facies F5, although fully bioturbated, shows remnants of parallel lamination. Unlike the planar laminated sandstone of facies F7, the fully bioturbated nature suggests bottom-current velocities that sustained environmental conditions suitable for burrowing organisms. As such, and since the sand fraction is generally coarse-grained, the planar lamination and tabular bedding are more likely associated with the lower stage plane bed flow-regimes with current velocities between $0.4 \mathrm{~m~s^{-1}}$ and $0.6 \mathrm{~m~s^{-1}}$ (Southard & Boguchwal, 1990). Like the heterolithic sandstones of facies F4, this facies often forms the lateral equivalent of sub-facies F6.1 and F6.2, albeit associated with lower current velocities. As the flow velocity within bottom currents decreases laterally away from the core (de Weger *et al.*, 2021) this facies represents a lateral facies change related to an inter-channel depositional environment away from the core, towards the left channel flank (Fig. 7), or it was deposited at a time when the palaeo-MOW was diminished. *Macaronichnus*, the ichnogenera responsible for the fully bioturbated appearance of this facies, typically occurs in sand-rich shallow-marine (up to foreshore) high-energy settings (Seike *et al.*, 2011) but it has also, albeit scarcely, been identified in deeper environments (Rodríguez-Tovar & Aguirre, 2014). Based on the same

outcrops, Miguez-Salas & Rodríguez-Tovar (2021) explained the *Macaronichnus* trace maker activity in this deep environment by high-energy and nutrient-rich influxes related to strong bottom currents, generating similar environmental conditions to those in shallow-marine settings. The presence of *Scolicia*, usually associated with coarse silty to fine sandy sediment, is consistent with the availability of benthic food. The abundance and size of this trace, produced by irregular echinoids, increases with the amount and nutritious value of benthic food (Kröncke, 2006; Wetzel, 2008).

The cross-stratified nature and general tabular bedding of the unidirectionally migrating deposits of facies F6 suggests that they most likely constitute relics of deep-marine dunes. Based on the depositional domain in the slope and the evidence of a tidally modulated palaeo-MOW in the late Miocene (Capella *et al.*, 2017; de Weger *et al.*, 2020, 2021), these deposits are interpreted as sandy contourite dunes. Previously, facies F6 had been interpreted as two-dimensional (F6.1 and F6.2) and three-dimensional dunes (F6.3 and F6.4) by de Weger *et al.* (2020, 2021) related to vigorous bottom currents along the contourite channel. Similar facies have been reported by Nelson *et al.* (1993), Hernández-Molina *et al.* (2006) and Stow *et al.* (2013) in modern contourite channels. Based on grain size, sedimentary structures, the bedform-velocity matrix of Stow *et al.* (2009) as well as bedform-velocity flume experiments (Fedele *et al.*, 2016; Koller *et al.*, 2019; De Cala *et al.*, 2020), these bedforms have formed as unidirectionally migrating dunes under bottom current velocities reaching up to $1 \mathrm{~m~s^{-1}}$ (Table 1, Fig. 7). The regularly observed soft sediment deformation structures (Fig. 5G and I) consisting of overturned cross-strata (Type 1 *sensu* Allen & Banks, 1972) and fluid escape structures indicate disturbance whilst the sediments still contained water. According to Mckee *et al.* (1962), Brenchley & Newall (1977) and Owen (1996), tangential shearing drag on liquefied sand may produce these kinds of overturned folds. The fold-style of overturned cross-strata suggests that the deforming force was unidirectional in its action. The fluid escape structures with upward directed water-escape morphologies can be described as internally ruptured fluid-escape structures (*sensu* Owen, 1995). Since the water escape processes hardly involve foreset laminae but affected bed-sets, they likely did not originate during the migration of the sand dunes (Chiarella *et al.*, 2016).

The thinner-bedded, tabular, cross-stratified sandstones of F6.1 are more heterolithic in nature compared to F6.2, as foresets more distinctly alternate between more and less indurated sand. This alteration is the result of fining-upward foresets that are upward depleted in bioclastic material, likely resulting from alternating flow conditions, waxing and waning, most likely induced by tides (de Weger *et al.*, 2021).

The medium-bedded to thick-bedded cross-stratified sandstones of F6.2 represent higher energy, and more stable conditions of the palaeo-MOW compared to sub-facies F6.1 as they are thicker and more uniform in composition. Based on the bedform-velocity matrix by Stow *et al.* (2009), the bedform stability diagram by Southard & Boguchwal (1990) and the sedimentary structures of contourite deposits by Martín-Chivelet *et al.* (2008), flow velocities likely ranged between 0.4 m s^{-1} and 1.0 m s^{-1}.

The 3D dunes related to sub-facies F6.3 and F6.4 are, based on the bedform stability diagram by Southard & Boguchwal (1990), deposited by higher current velocities compared to the 2D dunes of sub-facies F6.1 and F6.2. The cyclic changes from angular to tangential toe-set geometries in F6.4 indicate cyclically changing, tidally modulated bottom current velocities.

The increasingly dominant occurrence of *Macaronichnus* and *Scolicia* between sub-facies 6.1 to 6.4 is consistent with the increase in bottom current velocities and available benthic food supply between these facies (Kröncke, 2006; Wetzel, 2008; Miguez-Salas & Rodríguez-Tovar, 2021). The intense bioturbation by *Macaronichnus* and *Scolicia* trace makers likely hampered bioturbation by other trace makers such as *Planolites* and *Thalassinoides*-like producers.

The planar laminated sandstones of facies F7 are always found below facies F6, regularly forming the lateral, towards the right channel flank, equivalent of F6. Due to its association with F6 and its inter-channel position, facies F7 is associated with the contourite channel and has a contouritic origin. Thin-section analysis on samples from F7.1 (KT1, KT2, KT3 and KT5) revealed that the very fine to fine-grained sand contains a significant number of pellets of reworked mudstone and glauconite, fine-grained shell fragments and predominantly planktonic foraminifera. The claystone pellets are likely sourced as rip-up clasts due to strong bottom current activity and the composition of this sand indicates winnowing. The long-axis of the bioclasts are oriented parallel to the bedding,

indicating primary current lamination. The planar parallel laminated beds with the presence of primary current lamination also suggest strong bottom currents, likely in the upper stage plane bed flow regime. Martín-Chivelet *et al.* (2008) reported similar facies in contourite deposits associated with current speeds ranging from 0.6 to 2.0 m s^{-1}. Based on the bedform stability diagram by Southard & Boguchwal (1990), flow velocities for the very fine to fine-grained sand in facies F7.1 were likely in the range of 0.6 to 1.0 m s^{-1}, whereas flow velocities for the medium-grained sand in facies F7.2 were likely in the range of 1.0 to 1.6 m s^{-1}. The bi-gradational nature of the beds and on a larger scale the bed-sets, most clearly observed in facies F7.1, suggest gradual changes in flow strength.

Like facies F5, this facies contains abundant trace fossils; however traces are predominantly undifferentiated, indicating that benthic food is mainly available on the seafloor, decreasing downward within the sediment. The presence of benthic food at the seafloor can indicate changes in flow strength, where during times of decreased flow velocities nutrients were preserved at the seafloor, favouring trace maker activity.

Since no clear facies indicative of turbidite deposits have been found within the contourite channel facies described here, it is most likely that currents were sufficiently strong and/or long-lasting to overprint, by reworking, potential turbidity deposits.

Gravity-driven flow deposits (FA4)

The convolute and/or contorted nature and the erosive basal surfaces of facies F8 (Table 1, Fig. 5H and I) suggests that it represents the product of a slump (Leeder, 2009; Reading, 2009; Shanmugam, 2010). The regular presence of fluid escape structures recognized directly below facies F8, most often occurring in facies F6, attests to the sudden displacement of sediment creating overpressure in the still water-bearing cross-stratified sandstones (F6). Although slumps may occur over a wide range of depositional environments, their formation mainly relies on inclined surfaces (for example, slopes). Since the primary bedding of facies F8 is like facies F6.3/F6.4 and F9, F8 might represent down-slope, plastically deformed dunes and fine-grained turbidites, respectively. As facies F8 with a composition like facies F6.3/F6.4 is predominantly found interbedded with facies

association FA3, these slumps might represent collapsed dunes. As facies F8 with a primary composition like facies F9 is primarily found on the right flank of the channel, here F8 likely represents slope deposits that slumped into the channel (Fig. 7), either due to oversteepening of the slope and/or tectonic instability or due to undercutting of the slope by the core of the bottom current. Mézerais *et al.* (1993) also observed that local sediment slumps occur on flanks of contourite channels and that sedimentation on these flanks was likely disrupted by slumps.

Facies F9 (Table 1) generally shows basal scours and clear bounding surfaces. The well-sorted to very well-sorted, normal graded beds and internal structures typically represent a decelerating turbulent flow from the upper flow regime to suspension fallout (Bouma, 1962). Facies F9, predominantly consisting of thin bedded turbidites might suggest a basinal (silty–sandy distal lobe) depositional setting. However, they more likely represent the tail of turbidity current deposits on the slope (Mutti, 1992; Mutti *et al.*, 2009; Mulder, 2011; Talling *et al.*, 2012) or very low-density turbiditic currents on the slope, as recently discussed by de Castro *et al.* (2020, 2021) and Hüneke *et al.* (2021) (Fig. 7).

The deeply incised erosional surface of facies F10 indicates high shear stresses likely related to very high flow velocities or dense flow. The nature of deposition suggests a clastic flow most likely resulting from slope instability. Some conglomerates enriched in quartzose clasts may be first-cycle deposits that formed by erosion of a quartzite, quartz arenite or chert-nodule limestone source (Boggs Jr & Boggs, 2009). The accretionary wedge, actively uplifting around the time of deposition and slope formation prior to the deposition of the studied sections, is composed of blocks of different lithologies (limestones, sandstones and evaporites among others, Sani *et al.*, 2007) and was thus likely the source of the debris-flow conglomerate.

Facies distribution within the contourite channels (FA3)

The second-order channels and their sedimentary facies distribution is referred to with respect to the position within the first-order channels. Terminology applied for both the first and second-order channels is provided in Fig. 8. In the Sidi Chahed outcrop the across channel direction is roughly north–south, whereas the

across channel direction in Kirmta is oriented north-east/south-west (Figs 9 and 10).

Besides the vertical facies stacking pattern logged throughout both outcrops (Figs 3 and 4), picture analysis and field sketches allow for the recognition and distribution of second-order channels as well as both vertical and lateral sedimentary facies changes (Figs 9 and 10). The detailed assignation of sub-facies from pictures proved difficult, resulting in only facies F6 and F7 being assigned. This does not significantly change the outcome of the interpretations. The first-order channels are dominantly encased by facies association 1. For all first-order channels the lower bounding surfaces are erosive (concave-up). The second-order channels with erosional, concave-up lower bounding surfaces, most clearly identified in the Sidi Chahed outcrop (Fig. 9), are mainly filled by facies association 3 but show a strong correlation to facies F8.

Sidi Chahed

In the Sidi Chahed section (Figs 3 and 9), the best visualization of the second-order channels, and their sedimentary facies distribution is applied for SU-1 (Fig. 9A to E); however, similar trends were observed in SU-2 and SU-3. Figure 9E represents the right, most proximal, flank of the channel, whereas Fig. 9D represents the left (more distal) flank of the channel. Figure 9C represents a location in the channel close to its axis (Fig. 8).

The right channel flank is dominated by turbidites (F8), which have a similar primary petrographic composition as the slump deposits (F9). This facies transitions laterally (towards the axis of the channel) towards planar laminated sandstones (F7.2) and cross-stratified sandstones (F6.4/F6.3 and F6.2) (Fig. 9E). The vertical facies signature in the right flank consists of the subsequent stacking of convolute sandstones (F8), separated by erosive bounding surfaces. In the direction towards the channel axis the vertical facies distribution consists of the successive stacking of F7.2, F6.3/F6.4 and F6.2. The overall vertical facies trend in the second-order channels is fining-upward, related to changes in facies with complex to more simple architectures and internal structures, grading from facies F8, F7 to F6.

The axis area of the channel (Fig. 9C) is marked by extensive second-order erosional surfaces with distinct changes in bedding orientation of the infill sequences. Similarly, to the right flank, the overall trend is fining-upward related to a vertical facies distribution that, in
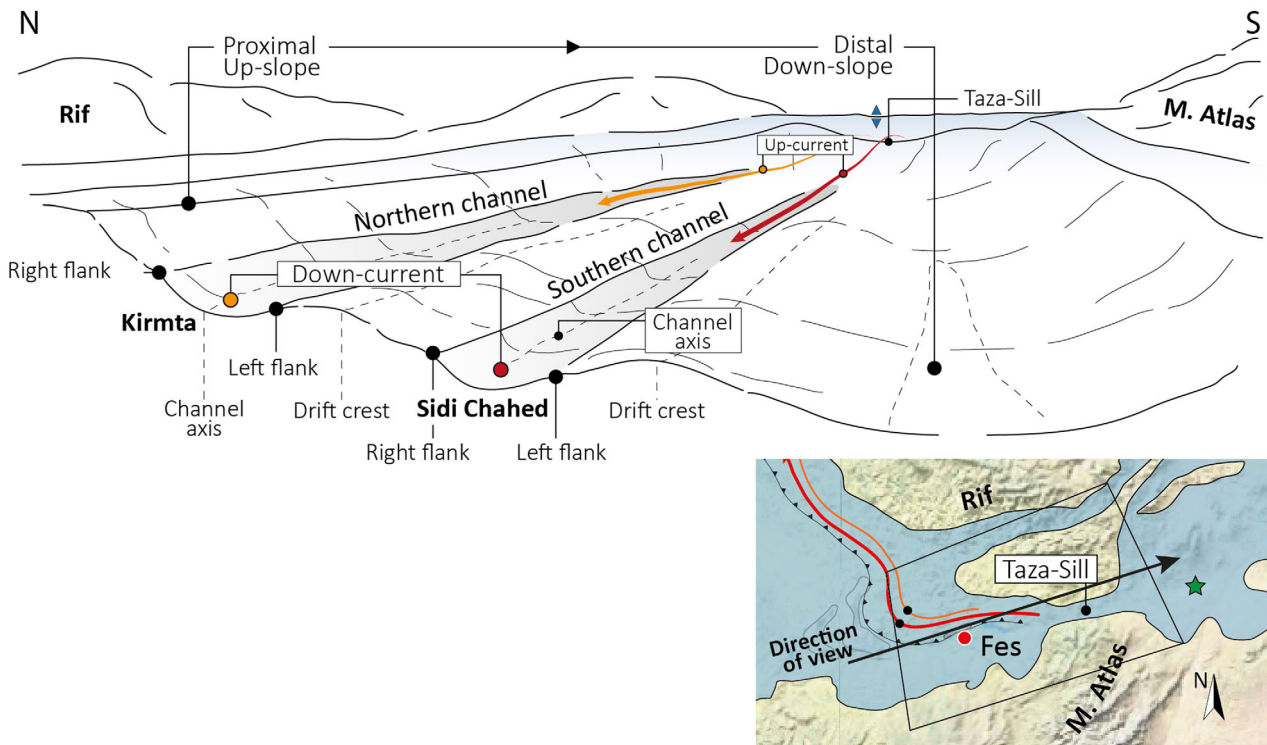
Fig. 8. Simplified palaeogeographical setting and terminology of the late Miocene, South Rifian Corridor contourite channel system. The panel in the lower right corner shows a reference frame with the direction of view (crop mask of Fig. 1).

general, consists of the subsequent stacking of F7.2, F6.3/F6.4 and F6.2. The lateral facies changes (towards the left flank) are marked by a modest change from dominantly higher, to lower order facies (F7 to F6).

The left flank of the channel (Fig. 9D) is marked by second-order channels with clear erosional lower bounding surfaces. Although these unconformities can also be identified in the previously discussed parts of the channel, here they are most prominent due to the asymmetrical evolution of the channel, migrating up-slope. The vertical facies distribution in this flank is marked by a change from dominantly higher to lower order facies (F6.4 to F3). The lateral facies changes are marked by a similar distribution (fining towards the left) albeit directed in a more distal direction, outside of the channel.

Below the left flank of the channel facies F8, F9 and F10 can be found as individual bodies encased in facies association 1 (Fig. 9D), not showing any process related lateral facies changes. Within the left flank of the channel, facies F8, which occurs interbedded with F6, shows internal features more like facies F6 than F9.

Kirmta

Within the Kirmta outcrop the three first-order channels (SUs) show good lateral and vertical exposure (Fig. 10A and B). The direction of view is roughly parallel to the flow direction and thus to the axis of the first-order channels. The erosive lower channel bounding surface is incised into facies association 1. This erosive bounding surface is overlain by sub-facies F7.1 which, in the axis of the channel, is overlain by another erosive bounding surface. On top of facies F7.1 stacked intervals of facies F6 (predominantly sub-facies F6.2) were found which are separated by laterally extensive, near vertical erosional surfaces. Facies F6 grades, quite rapidly, to the facies of FA2 and FA1, where FA1 is regularly interbedded by facies F9 (Fig. 10C).

Below the left channel flank of the first-order channel, facies association 1 coarsens upward, followed by the erosional lower bounding surface of the channel. At this location, the channel fill sequence consists of the stacking of facies F7.1, F6.1, F6.2 (erosive lower bounding surface) and F6.1 after which a fining-upward transition occurs from facies F4, F3, F2 to F1. Towards the

Fig. 9. Facies distribution within main Sand-Units (SU1–SU3) of the Sidi Chahed outcrop. (A) Panoramic picture with the main, concave-up sand units, indicated (from old to young), by the yellow (SU1), green (SU2) and red (SU3) lines. This colour-scheme is also applied to the remaining figures. (B) Top-view of the outcrop with the black arrows indicating the main palaeo-current direction and the dotted lines indicating the width of each sand unit. (C) Panoramic picture and interpretation of part of Sand-Unit 1 as indicated in (A). (D) The southern flank of Sand-Unit 1 and its interpretation. (E) The northern flank of Sand-Unit 1 and its interpretation.
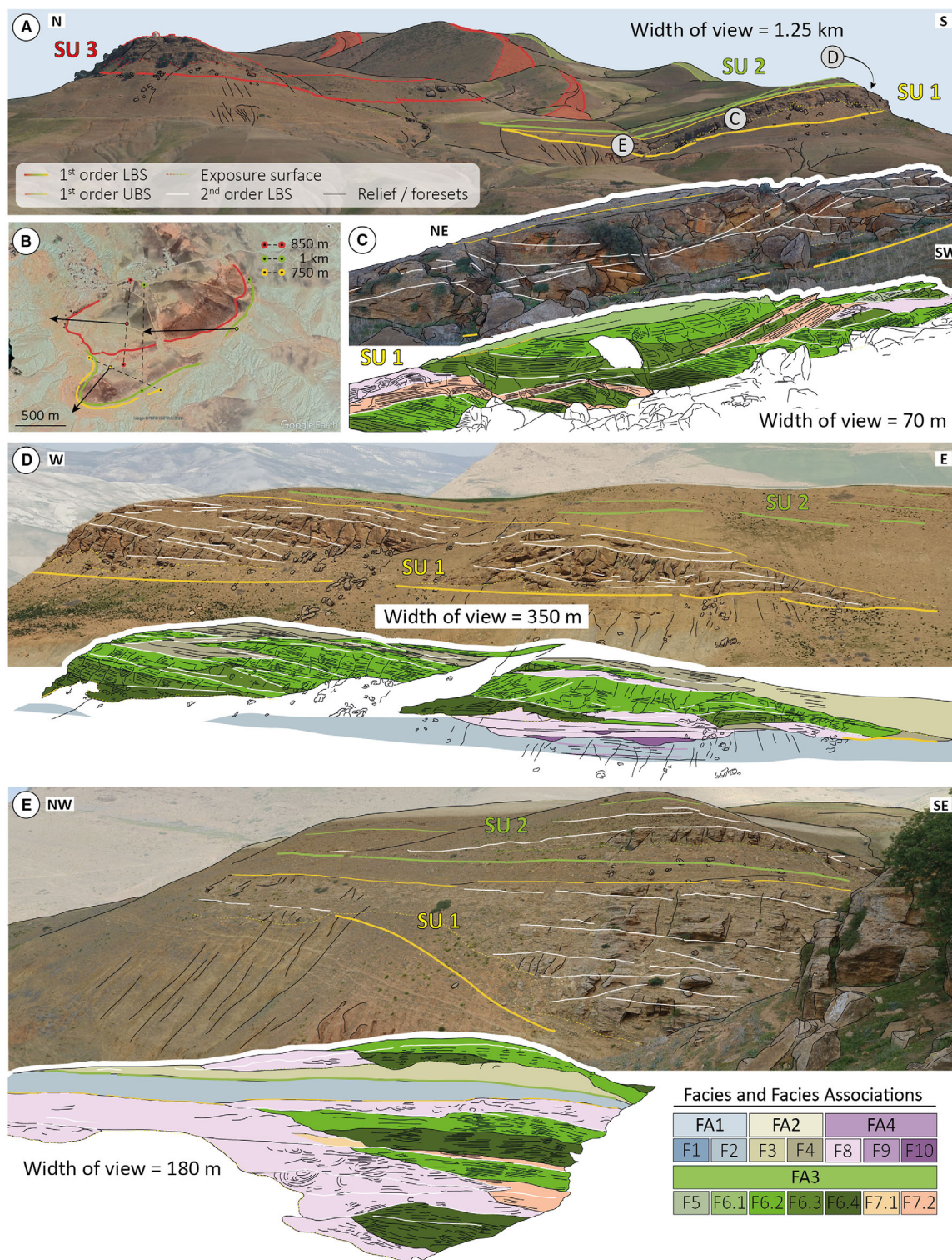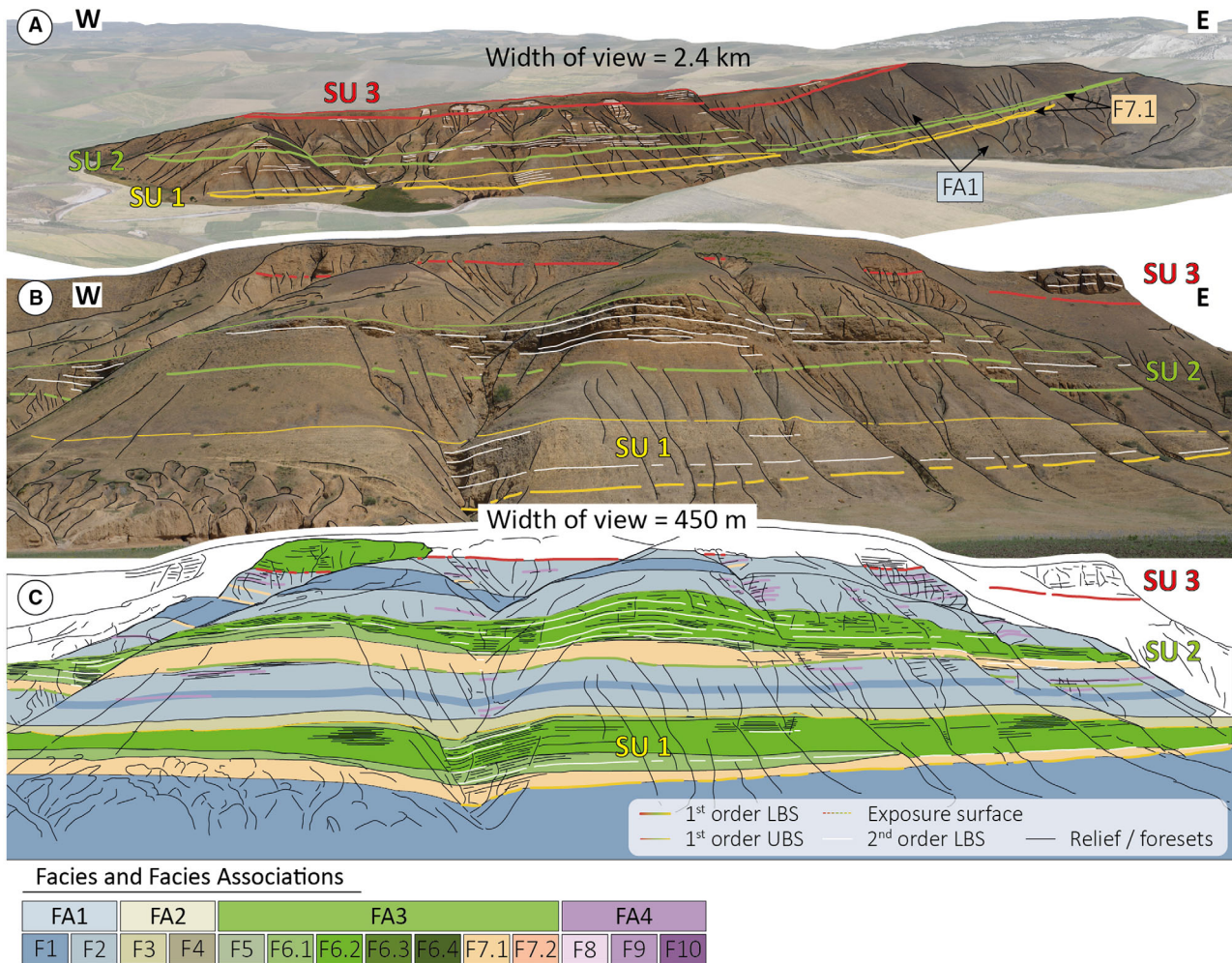
Fig. 10. Facies distribution within main sand-units (SU1–SU3) of the Kirmta outcrop. (A) Panoramic picture with the main, gently concave-up sand units, indicated (from old to young), by the yellow (SU1), green (SU2) and red (SU3). Facies in the east consist of laterally extensive F7.1 encased by facies association FA1. (B) Panoramic of the middle part of the outcrop with (C) the facies distribution interpretation below.

axis of the channel the main lateral facies change consists of a thicker interval of facies F6.2, which, towards the left flank grades to FA3 (Fig. 10C). The right flank in the east (Fig. 10A) is less complex, only consisting of slightly coarsening-upward facies association 1, followed by the presence of cyclically stacked bed-sets of F7.1 (Fig. 4D).

DISCUSSION

De Weger *et al.* (2020) investigated the spatial distribution and time variations between sand units in the Sidi Chahed and Kirmta sections, which were interpreted as two separate

contourite channels related to the late Miocene Contourite Channel system. Similarities have been observed in analogue channels which have developed in the Gulf of Cádiz since the opening of the Strait of Gibraltar (Hernández-Molina *et al.*, 2014; Llave *et al.*, 2020). At the exit of the Strait of Gibraltar, the contourite depositional system, formed by the circulation of the Mediterranean Outflow Water (MOW) since the early Pliocene to the present (Hernández-Molina *et al.*, 2014), consists of a succession of deeply incised valleys/channels, channel fills and mounded drifts (Fig. 11). De Weger *et al.* (2020) recognized that the palaeo-MOW acted in a similar way as the present-day MOW, which also consisted of two branches: (i) the upper,

shallower northern channel/branch related to the Kirmta outcrop; and (ii) the lower, deeper southern channel/branch related to the Sidi Chahed outcrop. Both branches of the palaeo-MOW were deflected towards the right (north) by the Coriolis force. The upper branch resulted from the partial mixing of intermediate and deep Mediterranean waters, whereas the lower branch consisted of deep Mediterranean waters (*sensu* Hernández-Molina *et al.*, 2014), resulting in relatively lower/higher density gradients and lower/higher flow velocities for the upper/lower branches, respectively. Because this interpretation of the large morphological features is adopted herein, most sedimentary facies are associated with the contourite channel or adjacent drift (Fig. 7).

First-order contourite channels

The first-order contourite channels are the largest concave-up, purely erosional features, forming the marl/sand interface, in the frontal part of the accretionary wedge (Fig. 12). De Weger *et al.* (2020) suggested that these first-order contourite channels migrated up-slope from SU1 to SU3, driven by tectonic activity. Based on the

study case of the Gulf of Cadiz, the southern channel is influenced by the present-day lower core of the MOW, conditioned both by tectonics and glacioeustatic changes in sea level. In the Gulf of Cadiz, the first-order channels are on average 3 to 4 km wide, about 160 km long and are between 30 to 50 m incised, much like the observed channel fill sequences in the ancient record (35 m). In the Gulf of Cadiz, several channel erosive discontinuities (C_1 to C_9 in Fig. 11) and their respective smaller incisions with sedimentary infill units (second-order channels) are described, developing since their inception in the early Pliocene. Five of these channels (C_1 to C_5) have developed in the central depression between two structural highs, the western high being the hanging wall of a thrust fault. During the early Quaternary to late Pleistocene, there was a clear displacement of three erosive channels (C_6 to C_8) as well as the formation of adjacent smooth mounded drifts on their western sides (Fig. 11). These channels and associated mounded drifts have migrated up-slope to their present-day location. This mode of up-slope migration is similar to that observed in the Kirmta and Sidi Chahed outcrops (SU1 to SU3). The youngest channel (C_9)
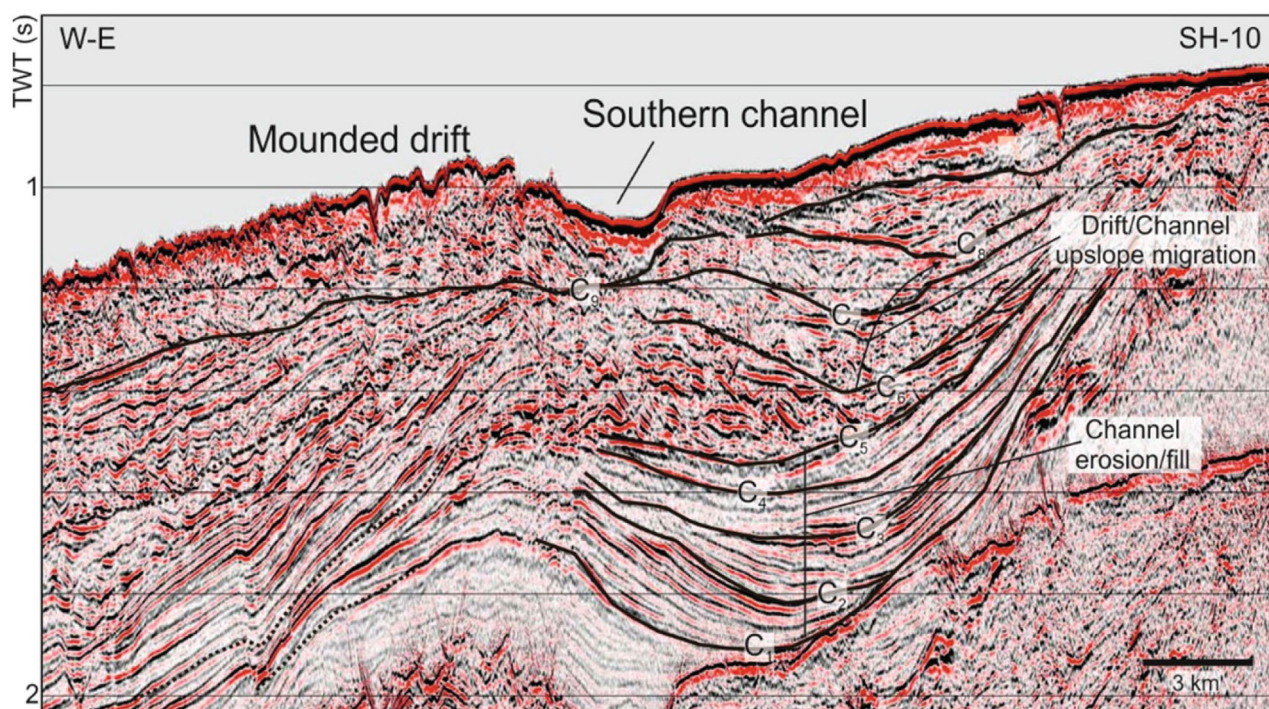

Fig. 11. Multichannel seismic profile from the Gulf of Cadiz contourite depositional system showing the distribution of the erosive base of contourite channels developed coeval with regional discontinuities (from old to young; C_1 to C_9). Seismic line provided by REPSOL Exploration, S.A.

has been laterally displaced towards the north-west during the Late Pleistocene up to present (Fig. 11).

Besides a tectonic origin for channel migration, tectonism is also assumed to be intimately related to the behaviour of the palaeo-MOW due to the formation and evolution of the Taza-Sill. The purely erosive nature of the palaeo-MOW in its phase of first-order contourite channel formation is related to very vigorous bottom currents. Since the first-order contourite channels are larger than the second-order channels, the core of the palaeo-MOW during this stage was larger and likely more confined (Fig. 12). The initiation of bottom currents is believed to have coincided with large density differences between the palaeo-MOW and the ambient water due to enhanced Mediterranean deep-water formation as a result of increased restriction of water-mass exchange. Furthermore, the density gradient was thought to be very high as the ambient water mass and the palaeo-MOW were not yet diluted by turbulent mixing. This high-density gradient not only resulted in very vigorous currents, but it also resulted in a large, confined core. These factors are likely the reason why the initial phase of contourite channels is usually marked by large erosive channelized surfaces (Faugères *et al.*, 1999; Llave *et al.*, 2006; García *et al.*, 2009; Hernández-Molina *et al.*, 2014; Gong *et al.*, 2017).

In the literature it is well-established that the current velocities of overflow water are highest near the point of overflow, decelerating due to turbulent mixing and topographic gradient changes down current (Sánchez-Leal *et al.*, 2017). The distribution of facies in agreement with this model have also been documented in ancient Mediterranean Straits (for example, Catanzaro Strait; Longhitano *et al.*, 2012). This suggests that both the Sidi Chahed and Kirmta outcrops were in close to the sill.

The transition from a purely erosive, towards a more depositional system is most likely primarily related to a decrease in flow velocities resulting from turbulent mixing with the ambient water masses. Furthermore, upon establishment of two-way exchange, related to the initiation of overflow water associated with the formation of the first-order channel, the density of the palaeo-MOW decreased as it became less restricted. Sediment supply should not have been a controlling factor because tectonic activity, a major constituent for down-slope sediment supply, is thought to have played the dominant role during this phase of contourite channel formation.

Reconfiguration of the Taza-Sill, its effect on the behaviour of the palaeo-MOW and the southward migration of the accretionary wedge are all primarily deemed responsible for the step-wise formation of the six identified first-
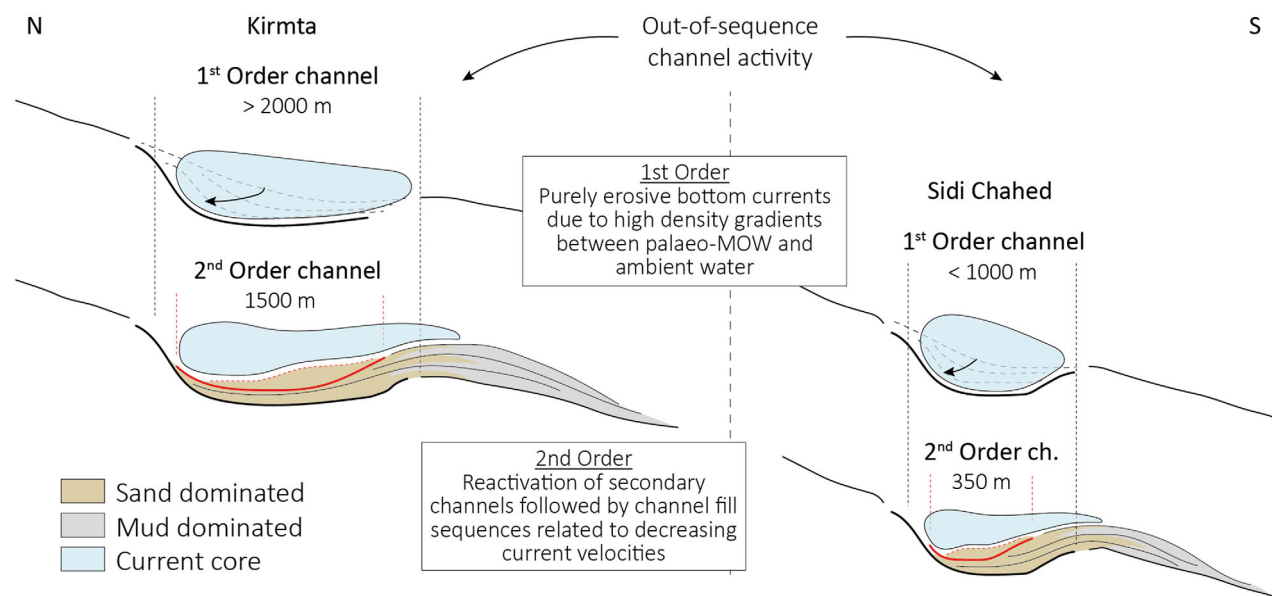

Fig. 12. Sketch of the Sidi Chahed and Kirmta sections within the slope. This sketch furthermore depicts the first and second-order channels, their morphologies, and their interrelationship.

order contourite channels (de Weger *et al.*, 2020). Observations from the Gulf of Cadiz Contourite System have shown that a stronger MOW in the deeper channel is linked to glacial periods, associated with higher aridity in the Mediterranean and thus an increase in the density of Mediterranean Deep Water (Llave *et al.*, 2006). De Weger *et al.* (2020) implied from this that the MOW favours either the upper or lower channel due to changes in density characteristics of the palaeo-MOW and that they are not synchronously active. Accordingly, such changes are induced by tectonic and climatic processes and their effects on the Mediterranean water masses. The late Miocene however was not severely affected by glacial–interglacial (eccentricity) cycles but was more dominantly affected by precession (Sierro *et al.*, 1999). Precessional cyclicity is therefore thought likely to have been a secondary driving force behind the first-order intermittent behaviour of the palaeo-MOW (Sierro *et al.*, 2020) and the out-of-sequence behaviour of the channel branches, or it controlled the second-order contourite channel features. Smaller-order changes in the hydrodynamic characteristics of the palaeo-MOW are related to millennial and seasonal changes in climatic conditions (Gladstone *et al.*, 2007) and due to the short timescales that primarily affected channel fill sequences.

Second-order contourite channels

The second-order contourite channels are characterized by smaller scale erosional channels that have subsequently been filled with sediment, making them both erosional and depositional. The formation of these second-order channels is initiated by erosive reactivation events after which deposition took place. This change from an erosional to a depositional regime is mainly due to a decrease in flow velocity of the palaeo-MOW and/or increased down-slope sediment supply to the channel. The reason why these second-order channels are more easily identified in the Sidi Chahed section might be because, in general, this section was influenced by more vigorous bottom currents and thus also stronger erosive events.

The spatiotemporal infill of the secondary channels is primarily related to the velocity distribution of bottom current water masses. Highest bottom current velocities are found in the core of the bottom current with decreasing current velocities towards the left flank (dependent on the deflection caused by the Coriolis force) and the drift (Fig. 7). Depending on sediment availability, sediment characteristics and the velocity of the current, bedforms are identified to have been developed in accordance with the bedform stability diagram (Southard & Boguchwal, 1990). The full range of across channel facies/bedforms identified in the Sidi Chahed outcrop (Fig. 7), from the right to the left flank, consist of slope erosion, upper-stage plane bedforms (or part of larger wavelength bedforms in upper stage) (F7), three-dimensional dunes (F6.4 and F6.3), two-dimensional dunes (F6.2 and F6.1), lower-stage plane bedforms, and heterolithic, transitional facies (F4). The channel-drift transitional facies of F4 cover both the left flank of the channel and the adjacent drift. The channel-drift transitional facies F3 is located close to the drift and transitions to pure drift facies F2 and F1 in a distal direction (Figs 7 and 13).

The panoramic pictures of the Sidi Chahed outcrop (Fig. 9) clearly show the stepwise reactivation of the bottom current, recognized by second-order channel migration. The secondary channels are recognized to either prograde (move up) or retrograde (move down) with respect to the lateral palaeo-slope.

Progradation, or the distal migration of the second-order channel with respect to the slope, is usually associated with large slump deposits in the right flank. These slump deposits, by occupying the right flank area of the channel, likely forced the core of the current in the direction of the left flank, forcing progradation or southward channel migration (Fig. 13A). These slumps were either triggered by tectonic instability or undercutting by the core of the bottom current. Progradation could also be stimulated by higher density contrasts between the bottom current and the ambient water mass, allowing the core to flow deeper, down slope. Retrogradation represents the normal evolution of contourite channel systems (Faugères & Stow, 2008), where erosion occurs on the right flank and deposition is focused on the left flank and the adjacent drift, forcing the system to migrate towards the right or up-slope. The observed secondary channel distribution comprises the subsequent progradation and retrogradation of the contourite channel. This evolution indicates that, if the slumps were triggered by tectonic induced instability, the system was initially affected by stronger/more frequent tectonic activity. These tectonic pulses decreased

roughly half-way during the evolution of the channel, decreasing sediment slumping, and causing the system to prograde. The final stages of channel fill are marked by the presence of relatively fine-grained and thinner bedded deposits (Figs 3 and 4), indicating a decrease in flow velocity (Fig. 7). This decrease in flow velocity likely resulted from a decrease in the density gradient between the palaeo-MOW and the ambient water masses.

The facies distribution in the Kirmta outcrop is distinctly different from that in the Sidi Chahed outcrop and second-order channels are hardly recognized. Despite the lack of distinct second-order channels, within the facies distribution several laterally extensive and near horizontal reactivation surfaces have been recognized. These reactivation surfaces are expected to have resulted from either a decrease in sediment transported to the system or temporary flow velocities exceeding that required for sediment deposition. These features were triggered by similar processes as those described for the Sidi Chahed outcrop.

Mechanics of dense gravity flows

The MOW flowing down the Taza-Sill and through the channels can be regarded as a dense (saline) gravity flow driven not only by the density gradient established with the water mass above, but also the topographic gradient down the sill. The dense, energetic bottom flow will entrain water from above due to friction and turbulent mixing at the interface and develop a lower boundary layer in contact with the seabed, the thickness of which is controlled by the relative importance between bed and interface friction (Fedele *et al.*, 2016; Koller *et al.*, 2019; De Cala *et al.*, 2020). It is important to keep in mind that, although some of the hydrodynamic and sediment transport processes associated with dense bottom flows might not be fully analogous to the subaerial (fluvial) case, some
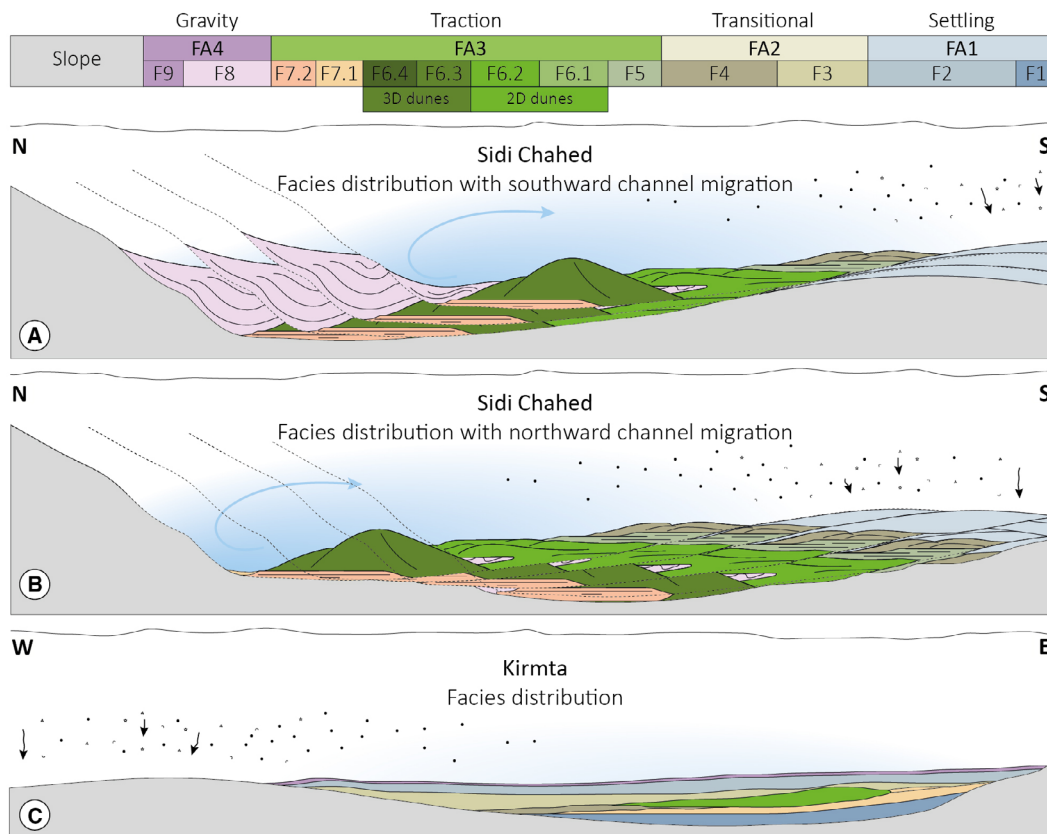

Fig. 13. Evolution of second-order channels and their related infill deposits. The secondary channels within the Sidi Chahed section (A) and (B) either prograde (A) or retrograde (B). The channel fill sequence in the Kirmta section is less complex due to weaker bottom currents and smaller bottom current velocity fluctuations.

fundamental behaviour related to particularities of bedform dynamics remain common to many different flow types, such as for example the relationship between dune and turbulent boundary layer mechanics (Fedele *et al.*, 2016). The thickness of the lower boundary layer of the MOW flowing through the channels is estimated to be within the range of 8 to 14 m, using scaling from the observed dune properties (wavelength, height, grain size; Kennedy, 1969; Engelund, 1970; Raudkivi, 1976; Yalin, 1977; Fedele *et al.*, 2016). Assuming well-developed dunes, dune heights of about 2 to 3 m and sediments ranging 250 to 500 μm, would indicate dune wavelengths on the order of 40 to 70 m. In addition, estimates of shear velocities and thus dimensionless shear stresses (Shields – or mobility parameter) of about 0.4 to 0.6 (Liu, 1957; van Rijn, 1984; Van den Berg & Van Gelder, 1993; Parker, 2008) lead to a range of bed-related friction coefficients C_f of the flows in the range 0.007 to 0.01. Bed-related friction coefficients are then increased appropriately to account for the contribution of interfacial friction and mixing in the dense gravity flow (Ellison & Turner, 1959; Streeter & Kestin, 1961), to obtain estimates of the current average velocity, thus found in the range 0.6 to 0.9 m s^{-1}.

Although very similar to previous estimates described above using dimensioned bedform diagrams (Boguchwal & Southard, 1990), the latter are derived and consistent with a more realistic flow setting. Finally, using these average flow velocities and thickness of the boundary layer, along with a range of fractional density differences between the dense lower cascading flow in the MOV and the water mass above of the order of 0.001 to 0.005, densimetric Froude numbers applicable to the lower boundary layer are computed and found to be in the order of 1.5 to 1.9 (supercritical). The Froude estimates and grain sizes observed place the bedforms in the appropriate field of stability of dunes created by dense gravity flows, reported in Fedele *et al.* (2016), Koller *et al.* (2019) and De Cala *et al.* (2020).

Facies model

Based on the current findings, the sedimentary facies model for sandy contourites, previously proposed by de Weger *et al.* (2021), requires the addition of a down-current dimension (Fig. 14). The range of erosional morphologies and depositional sedimentary facies both depend on, as stated previously: (i) sediment availability; (ii) the

characteristics of the available sediment; and (iii) the hydrodynamic characteristics of the water mass that forms a bottom current with respect to the hydrodynamic characteristics of the ambient water mass.

In general, the velocity of bottom currents decreases in two directions, both down current and away from the core of the current in the opposite direction to which the core is deflected by the Coriolis force (Fig. 14). The formation of bedforms follows this down-current and core-perpendicular trend in decrease in flow velocities depending on the grain size and current velocity. Despite bedform stability diagrams being deduced from tank-experiments, the evolution of the documented bedforms associated with a decrease in flow velocity in outcrop, although limited by the availability of sediment and its characteristics, correlate well to these diagrams.

If current velocities and sediment availability are all appropriate, a full range of bedforms might develop in contourite channels. If flow velocities are lower, either due to a decrease in the density difference between the water mass of the bottom current and the ambient water mass, turbulent mixing of the water masses, or other processes affecting a decrease in flow velocities, the depositional regime changes. An example of this change is likely recorded between the Sidi Chahed and Kirmta outcrops, where the Kirmta outcrop was affected by weaker current velocities. On the other hand, morphological features such as obstacles and confinement can increase current velocities, causing a shift in bedforms related to higher flow velocities.

Facies model applicability

Published evidence of sandy contourite deposits, primarily located in the Gulf of Cadiz (Hernández-Molina *et al.*, 2006; Stow *et al.*, 2013; Hernández-Molina *et al.*, 2014; Brackenridge *et al.*, 2018; de Castro *et al.*, 2021) but also in Faero Bank Channel area (Akhmetzhanov *et al.*, 2007), the South China Sea (Gong *et al.*, 2017), onshore in the Yangtze region of China (Zhang *et al.*, 2020) and in the southern Brasil Basin (Mézerais *et al.*, 1993), reveals that contourite channel deposits are primarily found in areas in which the contourite channel changes its orientation, forming a bend. The studied sections, due to the obstruction of the Prerif Ridges (Fig. 1; de Weger *et al.*, 2020), were likely also located in an area where the contourite channel formed a bend. The scarcity
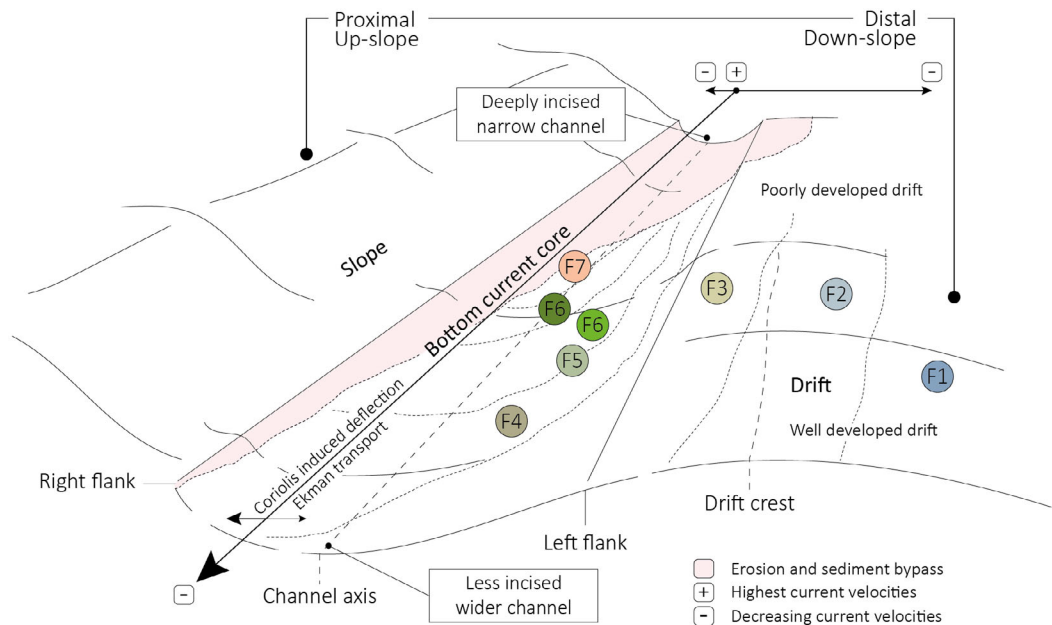
Fig. 14. Three-dimensional sandy contourite facies model showing the contourite channel and drift. Up current, or at the site of overflow, bottom current velocities are highest. Down-current bottom current velocities decrease. The bottom current core is the most energetic part within contourite systems, with decreasing current velocities away from the core. This model represents an idealized facies model where the facies distribution is a product of both sediment characteristics and current velocities.

of recognized contourite channel deposits and the fact that, where recognized, the contourite channel depositional features are located in bends of the channel suggest that sedimentation in contourite channels might primarily take place within these bends, and/or that the preservation potential is highest in these areas. Consequently, contourite channels in outcrop might only be recognized/preserved at bends. The factors behind this phenomenon are likely related to changes in flow characteristics. Piper & Normark (1983) mentioned that flow stripping happens mostly in the bends of turbidite channels and otherwise most of the flow is concentrated within the channel. Similar as for turbidite channels, flow stripping might be responsible for the change in flow characteristics in the bends of contourite channels and their associated deposits. Thus far, the processes behind the change in flow characteristics responsible for preferred deposition in bends (such as cross-flows resulting from the combined action of Coriolis effect, slope gradient and bottom Ekman layers) can only be hypothesized and thus need to be investigated further. The proposed facies model however is still viable because it is primarily related to down-current and core lateral

decreases in flow velocity. It is possible though that the coarsest grained sedimentary facies are only found in areas of the contourite channel where it changes its orientation.

IMPLICATIONS

Climate reconstruction

Contourite systems are controlled by climatic processes. These climatic processes are captured in the sedimentary record. Particularly, sandstone contourite facies are prone to capturing even small-scale changes in flow characteristics induced by climatic change (de Weger *et al.*, 2021). By unravelling these signatures in the ancient record, the information contained within can help develop to understanding in changes in global ocean circulation. Inversely, as is the case for the palaeo-MOW, bottom-currents in gateways, or overflows, can significantly contribute to the thermohaline circulation (Rahmstorf, 2006; Kuhlbrodt *et al.*, 2007; Rogerson *et al.*, 2012), significantly affecting global climate. By studying contourite deposits we can improve the detailed resolution of fluxes of

dense overflow water and its contribution to global ocean circulation (de Weger *et al.*, 2020).

Reservoir potentiality

Contourite channels associated with lateral drifts and terraces have been recognized to contain large volumes of well-sorted sands in contourite depositional systems (Viana, 2008; Mutti & Carminatti, 2011; Stow *et al.*, 2013; Hernández-Molina *et al.*, 2016; Brackenridge *et al.*, 2018; de Weger *et al.*, 2021). These systems however were, as of yet, not well-understood, and the inter-channel and down-channel facies distribution had not yet been documented. This facies distribution however plays a vital role in the characterization and appraisal of sandy contourite reservoirs. Based on this study's findings, areas affected by overflows at the exits of straits, corridors and gateways develop sandy deposits in contourite channels where porosities within the inter-channel sandstone facies range between 2% and 25% (Table 2), albeit that porosity estimates might be enhanced by dissolution. These values however are based on microfacies MF1 and MF2, not including the coarser grained MF3 which has shown porosities up to 35%. Despite these preliminary results of reservoir quality, extensive petrophysical analysis on fresh rock samples should be executed.

One of the most promising features from the prospective of hydrocarbon system's potential is the association of the sand prone contourite channel fill and the adjacent mud prone contourite drift. The contourite drift has a high mud-to-sand ratio which likely has good characteristics to act as seal (Viana *et al.*, 2007; Viana, 2008; Bailey *et al.*, 2021). Based on the findings of this study, the first-order contourite channels, filled by sandstone facies (F5, F6 and F7), are encapsulated by muddy drift deposits (F1, F2, F3 and F4), indicating that the system is self-sealing.

CONCLUSIONS

This contribution focuses on the description and interpretation of relics of late Miocene contourite channels in outcrop that have formed by the action of overflow of the palaeo-Mediterranean Outflow Water (MOW). These channels consist of first-order contourite channels that range in width between 750 m and

2000 m and are up to 35 m deep. These first-order channels have formed by vigorous, erosive bottom currents associated with the tectonically induced initial phase of overflow formation. Subsequently, the first-order channels, that formed intra slope sub-basins, are filled by up to 300 m wide and up to 15 m deep second-order channels. These second-order channels represent a phase of erosion, followed by the deposition of sediment associated with a relative decrease in flow velocity. Migration of the second-order channels is partly controlled by tectonic instability, evidenced by slumps in the proximal part of the channel. The emplacement of slump deposits might have forced the core of the bottom current (or second-order channel) to migrate down-slope. The contourite channel migration is directed up-slope because of the combined effects of the Coriolis forces along with general up-slope erosion and down-slope accretion.

The depositional phase of the second-order channels is marked by sandstone deposits with traction structures associated with tidally modulated bottom currents generated by the palaeo-MOW. Changes in sedimentary facies are primarily related to short-term, tidally, seasonally and orbitally induced changes in the overflow characteristics, and the resulting changes in the velocity of the palaeo-MOW. Both down-current and across-channel facies changes from planar laminated sandstones (F7), three-dimensional dunes (F6.4 and F6.3), two-dimensional dunes (F6.2 and F6.1) to fully bioturbated sandstones with remnants of planar lamination (F5) are ascribed to a decrease in flow-velocity resulting from a decrease in acceleration due to gravity and the across-channel velocity profile, respectively. As such, the inter-channel sandstone facies correlate well to bedform stability diagrams.

This work comprises a novel, detailed study of an exposed contourite channel system from which a facies model for contourite channels is proposed. However, it needs to be carefully compared to other modern and ancient contourite depositional systems to increase its validity. Contourite channel deposits contain valuable, high-resolution information regarding the evolution of overflow-processes and their effect on changes in global ocean circulation. Coarse-grained contourite channels, such as those documented here, form potentially valuable reservoir targets in exploration geosciences. The documentation of coarse-grained contourite channel facies being limited only to bends in the contourite channel

might indicate that hydrocarbon reservoirs related to contourite channels are axially discontinuous.

REFERENCES

Akhmetzhanov, A., **Kenyon, N.H.**, **Habgood, E.**, **Van Der Mollen, A.S.**, **Nielsen, T.**, **Ivanov, M.** and **Shashkin, P.** (2007) North Atlantic contourite sand channels. *Geol. Soc. Lond. Spec. Publ.*, **276**, 25–47.

Allen, J.R.L. (1982) Mud drapes in sand-wave deposits: a physical model with application to the Folkestone Beds (early Cretaceous, southeast England). *Phil. Trans. Roy. Soc. London. Series A, Math. Phys. Sci.*, **306**, 291–345.

Allen, J.R.L. and **Banks, N.L.** (1972) An interpretation and analysis of recumbent-folded deformed cross-bedding. *Sedimentology*, **19**, 257–283.

Bailey, W., **McArthur, A.** and **McCaffrey, W.** (2021) Sealing potential of contourite drifts in deep-water fold and thrust belts: examples from the Hikurangi margin, New Zealand. *Marine Petrol. Geol.*, **123**, 104776.

Barbero, L., **Jabaloy, A.**, **Gómez-Ortiz, D.**, **Pérez-Peña, J.V.**, **Rodríguez-Peces, M.J.**, **Tejero, R.**, **Estupiñán, J.**, **Azdimousa, A.**, **Vázquez, M.** and **Asebriy, L.** (2011) Evidence for surface uplift of the Atlas Mountains and the surrounding peripheral Plateaux: combining apatite fission-track results and geomorphic indicators in the Western Moroccan Meseta (coastal Variscan Paleozoic basement). *Tectonophysics*, **502**, 90–104.

Blanc, P.L. (2002) The opening of the Plio-quaternary Gibraltar Strait: assessing the size of a cataclysm. *Geodin. Acta*, **15**, 303–317.

Boggs, S., Jr. and **Boggs, S.** (2009) *Petrology of Sedimentary Rocks*. Cambridge University Press, Cambridge.

Boguchwal, L.A. and **Southard, J.B.** (1990) Bed configurations in steady unidirectional water flows; part 1, scale model study using fine sands. *J. Sediment. Res.*, **60**, 649–657.

Bouma, A.H. (1962) *Sedimentology of Some Flysch Deposits: A Graphic Approach to Facies Interpretation*, p. 168. Elsevier, Amsterdam.

Brackenridge, R.E., **Stow, D.A.V.**, **Hernández-Molina, F.J.**, **Jones, C.**, **Mena, A.**, **Alejo, I.**, **Ducassou, E.**, **Llave, E.**, **Ercilla, G.**, **Nombela, M.A.**, **Perez-Arlucea, M.** and **Frances, G.** (2018) Textural characteristics and facies of sand-rich contourite depositional systems. *Sedimentology*, **65**, 2223–2252.

Brenchley, P.J. and **Newall, G.** (1977) The significance of contorted bedding in upper Ordovician sediments of the Oslo region, Norway. *J. Sediment. Res.*, **47**, 819–833.

Candela, J. (2001) Mediterranean water and global circulation. *Int. Geophys.*, **77**, 419–XLVIII.

Capella, W., **Hernández-Molina, F.J.**, **Flecker, R.**, **Hilgen, F.J.**, **Hssain, M.**, **Kouwenhoven, T.J.**, **van Oorschot, M.**, **Sierro, F.J.**, **Stow, D.A.V.**, **Trabucho-Alexandre, J.**, **Tulbure, M.A.**, **de Weger, W.**, **Yousfi, M.Z.** and **Krijgsman, W.** (2017) Sandy contourite drift in the late Miocene Rifian corridor (Morocco): reconstruction of depositional environments in a foreland-basin seaway. *Sed. Geol.*, **355**, 31–57.

Capella, W., **Barhoun, N.**, **Flecker, R.**, **Hilgen, F.J.**, **Kouwenhoven, T.**, **Matenco, L.C.**, **Sierro, F.J.**, **Tulbure, M.A.**, **Yousfi, M.Z.** and **Krijgsman, W.** (2018) Data on lithofacies, sedimentology and palaeontology of South Rifian Corridor sections (Morocco). *Data Brief*, **19**, 712–736.

Chalouan, A., **Michard, A.**, **El Kadiri, K.**, **Negro, F.**, **de Lamotte, D.F.**, **Soto, J.I.** and **Saddiqi, O.** (2008) The rif belt. In: *Continental Evolution: The Geology of Morocco*, pp. 203–302. Springer, Berlin Heidelberg.

Chiarella, D. (2016) Angular and tangential toeset geometry in tidal cross-strata: An additional feature of current-modulated deposits. In: *Contributions to Modern and Ancient Tidal Sedimentology: Proceedings of the Tidalites 2012 Conference*, Vol. 47, pp. 185–195. IAS Special Publication, Hoboken, NJ.

Chiarella, D., **Longhitano, S.G.** and **Tropeano, M.** (2017) Types of mixing and heterogeneities in siliciclastic-carbonate sediments. *Mar. Petrol. Geol.*, **88**, 617–627.

Chiarella, D., **Moretti, M.**, **Longhitano, S.G.** and **Muto, F.** (2016) Deformed cross-stratified deposits in the Early Pleistocene tidally-dominated Catanzaro strait-fill succession, Calabrian Arc (Southern Italy): triggering mechanisms and environmental significance. *Sediment. Geol.*, **344**, 277–289.

De Cala, I., **Ohata, K.**, **Dorrell, R.**, **Naruse, H.**, **Patacci, M.**, **Amy, L.A.** and **McCaffrey, W.D.** (2020) Relating the flow processes and bedforms of steady-state and waning density currents. *Front. Earth Sci.*, **409**. https://doi.org/10.3389/feart.2020.535743

De Castro, S., **Hernández-Molina, F.J.**, **De Weger, W.**, **Jiménez-Espejo, F.J.**, **Rodríguez-Tovar, F.J.**, **Mena, A.** and **Sierro, F.J.** (2021) Contourite characterization and its discrimination from other deep-water deposits in the Gulf of Cadiz contourite depositional system. *Sedimentology*, **68**, 987–1027.

De Castro, S., **Hernández-Molina, F.J.**, **Rodríguez-Tovar, F.J.**, **Llave, E.**, **Ng, Z.L.**, **Nishida, N.** and **Mena, A.** (2020) Contourites and bottom current reworked sands: bed facies model and implications. *Mar. Geol.*, **428**, 106267.

Duan, T., **Gao, Z.**, **Zeng, Y.** and **Stow, D.** (1993) A fossil carbonate contourite drift on the lower Ordovician palaeocontinental margin of the middle Yangtze terrane,

Jiuxi, northern Hunan, southern China. *Sediment. Geol.*, **82**, 271–284.

Ellison, T.H. and Turner, J.S. (1959) Turbulent entrainment in stratified flows. *J. Fluid Mech.*, **6**, 423–448.

Engelund, F. (1970) Instability of erodible beds. *J. Fluid Mech.*, **42**, 225–244.

Expedition 339 Scientists (2012) Site U1389 summary. In: *IODP Expedition 339: Mediterranean Outflow*. Site Summaries. International Ocean Discovery Program [online].

Faugères, J.C. and Stow, D.A.V. (2008) Contourite drifts: nature, evolution and controls. *Dev. Sedimentol.*, **60**, 257–288.

Faugères, J.C., Stow, D.A.V., Imbert, P. and Viana, A. (1999) Seismic features diagnostic of contourite drifts. *Mar. Geol.*, **162**, 1–38.

Fedele, J.J., Hoyal, D., Barnaal, Z., Tulenko, J. and Awalt, S. (2016) Bedforms created by gravity flows. In: *Autogenic Dynamics and Self-Organization in Sedimentary Systems*, Vol. **106**, pp. 95–121. https://doi.org/10.2110/sepmsp.106

Feinberg, H. (1986) Les séries Tertiaires Des Zones Externes du Rif (Maroc): Biostratigraphie, paléogéographie et aperçu Tectonique. *Éditions du Service géologique du Maroc* (No. 315).

Flecker, R., Krijgsman, W., Capella, W., de Castro Martíns, C., Dmitrieva, E., Mayser, J.P., Marzocchi, A., Modestou, S., Ochoa, D., Simon, D., Tulbure, M., van den Berg, B., van der Schee, M., de Lange, G., Ellam, R., Govers, R., Gutjahr, M., Hilgen, F., Kouwenhoven, T., Lofi, J., Meijer, P., Sierro, F.J., Bachiri, N., Barhoun, N., Alami, A.C., Chacon, B., Flores, J.A., Gregory, J., Howard, J., Lunt, D., Ochoa, M., Pancost, R., Vincent, S. and Yousfi, M.Z. (2015) Evolution of the late Miocene Mediterranean–Atlantic gateways and their impact on regional and global environmental change. *Earth Sci. Rev.*, **150**, 365–392.

Flinch, J.F., Bally, A.W. and Wu, S. (1996) Emplacement of a passive-margin evaporitic allochthon in the Betic Cordillera of Spain. *Geology*, **24**, 67–70.

García, M., Hernández-Molina, F.J., Llave, E., Stow, D.A.V., León, R., Fernández-Puga, M.C. and Somoza, L. (2009) Contourite erosive features caused by the Mediterranean outflow water in the Gulf of Cadiz: quaternary tectonic and oceanographic implications. *Mar. Geol.*, **257**, 24–40.

Garcia-Castellanos, D., Estrada, F., Jiménez-Munt, I., Gorini, C., Fernández, M., Vergés, J. and De Vicente, R. (2009) Catastrophic flood of the Mediterranean after the Messinian salinity crisis. *Nature*, **462**, 778–781.

Gladstone, R., Flecker, R., Valdes, P., Lunt, D. and Markwick, P. (2007) The Mediterranean hydrologic budget from a late Miocene global climate simulation. *Palaeogeogr. Palaeoclimatol. Palaeoecol.*, **251**, 254–267.

Gong, C., Peakall, J., Wang, Y., Wells, M.G. and Xu, J. (2017) Flow processes and sedimentation in contourite channels on the northwestern South China Sea margin: A joint 3D seismic and oceanographic perspective. *Mar. Geol.*, **393**, 176–193.

Gonthier, E.G., Faugères, J.C. and Stow, D.A.V. (1984) Contourite facies of the Faro drift, gulf of Cadiz. *J. Geol. Soc. London, Spec. Pub.*, **15**, 275–292.

Harris, P.T. and Whiteway, T. (2011) Global distribution of large submarine canyons: geomorphic differences between active and passive continental margins. *Mar. Geol.*, **285**, 69–86.

Hernández-Molina, F.J., Llave, E., Preu, B., Ercilla, G., Fontan, A., Bruno, M., Serra, N., Gomiz, J.J., Brackenridge, R.E., Sierro, F.J., Stow, D.A.V., Garcia, M., Juan, C., Sandoval, N. and Mrnaliz, A. (2014) Contourite

processes associated with the Mediterranean outflow water after its exit from the strait of Gibraltar: global and conceptual implications. *Geology*, **42**, 227–230.

Hernández-Molina, F.J., Llave, E., Stow, D.A.V., García, M., Somoza, L., Vázquez, J.T. and Gardner, J. (2006) The contourite depositional system of the Gulf of Cadiz: a sedimentary model related to the bottom current activity of the Mediterranean outflow water and its interaction with the continental margin. *Deep-Sea Res. II Top. Stud. Oceanogr.*, **53**, 1420–1463.

Hernández-Molina, F.J., Soto, M., Piola, A.R., Tomasini, J., Preu, B., Thompson, P., Badalini, G., Creaser, A., Violante, R.A., Morales, E., Paterlini, M. and De Santa Ana, H. (2016) A contourite depositional system along the Uruguayan continental margin: sedimentary, oceanographic and paleoceanographic implications. *Mar. Geol.*, **378**, 333–349.

Hernández-Molina, F.J., Stow, D.A.V., Alvarez-Zarikian, C.A., Acton, G., Bahr, A., Balestra, B., Ducassou, E., Flood, R., Flores, J.A., Furota, S., Grunert, P., Hodell, D., Jimenez-Espejo, F., Kim, J.K., Krissek, L., Kuroda, J., Li, B., Llave, E., Lofi, J., Lourens, L., Miller, M., Nanayama, F., Nishida, N., Richter, C., Roque, C., Pereira, H., Sanchez Goñi, M.F., Sierro, F.J., Singh, A.D., Sloss, C., Takashimizu, Y., Tzanova, A., Voelker, A.H.L., Williams, T. and Xuan, C. (2014) Onset of Mediterranean outflow into the North Atlantic. *Science*, **344**, 1244–1250.

Hilgen, F.J., Bissoli, L., Iaccarino, S., Krijgsman, W., Meijer, R., Negri, A. and Villa, G. (2000) Integrated stratigraphy and astrochronology of the Messinian GSSP at Oued Akrech (Atlantic Morocco). *Earth Planet. Sci. Lett.*, **182**, 237–251.

Hovikoski, J., Uchman, A., Weibel, R., Nøhr-Hansen, H., Sheldon, E., Ineson, J., Bjerager, M., Therkelsen, J., Olivarius, M., Larsen, M., Alsen, P. and Bojesen-Koefoed, J. (2020) Upper cretaceous bottom current deposits, north-East Greenland. *Sedimentology*, **67**, 3619–3654.

Hsü, K.J., Montadert, L., Bernoulli, D., Cita, M.B., Erickson, A., Garrison, R.E., Kidd, R.B., Mèlierés, F., Müller, C. and Wright, R. (1977) History of the Mediterranean salinity crisis. *Nature*, **267**, 399–403.

Hsü, K.J., Ryan, W.B. and Cita, M.B. (1973) Late Miocene desiccation of the Mediterranean. *Nature*, **242**, 240–244.

Hüneke, H., Hernández-Molina, F.J., Rodríguez-Tovar, F.J., Llave, E., Chiarella, D., Mena, A. and Stow, D.A. (2021) Diagnostic criteria using microfacies for calcareous contourites, turbidites and pelagites in the Eocene–Miocene slope succession, southern Cyprus. *Sedimentology*, **68**, 557–592.

Ichaso, A.A. and Dalrymple, R.W. (2009) Tide-and wave-generated fluid mud deposits in the Tilje formation (Jurassic), offshore Norway. *Geology*, **37**, 539–542.

Iribarren, L., Vergés, J. and Fernàndez, M. (2009) Sediment supply from the Betic–Rif orogen to basins through Neogene. *Tectonophysics*, **475**, 68–84.

Janocko, M., Nemec, W., Henriksen, S. and Warchoł, M. (2013) The diversity of deep-water sinuous channel belts and slope valley-fill complexes. *Marine Petrol. Geol.*, **41**, 7–34.

Kennedy, J.F. (1969) The formation of sediment ripples, dunes, and antidunes. *Annu. Rev. Fluid Mech.*, **1**, 147–168.

Kolla, V., Posamentier, H.W. and Wood, L.J. (2007) Deep-water and fluvial sinuous channels—characteristics, similarities and dissimilarities, and modes of formation. *Marine Petrol. Geol.*, **24**, 388–405.

Koller, D., **Manica, R.**, **Borges, A.D.O.** and **Fedele, J.** (2019) Experimental bedforms by saline density currents. *Brazilian. J. Geol.*, **49**. https://doi.org/10.1590/2317-4889201920180118

Krijgsman, W., **Capella, W.**, **Simon, D.**, **Hilgen, F.J.**, **Kouwenhoven, T.J.**, **Meijer, P.T.**, **Sierro, F.J.**, **Tulbure, M.A.**, **van den Berg, C.**, **van der Schee, M.** and **Flecker, R.** (2018) The Gibraltar corridor: Watergate of the Messinian salinity crisis. *Mar. Geol.*, **403**, 238–246.

Kröncke, I. (2006) Structure and function of macrofaunal communities influenced by hydrodynamically controlled food availability in the Wadden Sea, the open North Sea, and the deep-sea. A synopsis. *Senckenbergiana Maritima*, **36**, 123–164.

Kuhlbrodt, T., **Griesel, A.**, **Montoya, M.**, **Levermann, A.**, **Hofmann, M.** and **Rahmstorf, S.** (2007) On the driving processes of the Atlantic meridional overturning circulation. *Rev. Geophys.*, **45**. https://doi.org/10.1590/2317-4889201920180118

Leeder, M.R. (2009) *Sedimentology and Sedimentary Basins: From Turbulence to Tectonics*. Blackwell Science Ltd.

Lirer, F., **Foresi, L.M.**, **Iaccarino, S.M.**, **Salvatorini, G.**, **Turco, E.**, **Cosentino, C.** and **Caruso, A.** (2019) Mediterranean Neogene planktonic foraminifer biozonation and biochronology. *Earth-Sci Rev.*, **196**, 102869.

Liu, H.K. (1957) Mechanics of sediment-ripple formation. *J. Hydraulics Div.*, **83**, 1197–1191.

Llave, E., **Hernández-Molina, F.J.**, **García, M.**, **Ercilla, G.**, **Roque, C.**, **Juan, C.** and **Stow, D.** (2020) Contourites along the Iberian continental margins: conceptual and economic implications. *Geol. Soc. Lond. Spec. Publ.*, **476**, 403–436.

Llave, E., **Schönfeld, J.**, **Hernández-Molina, F.J.**, **Mulder, T.**, **Somoza, L.**, **Del Río, V.D.** and **Sánchez-Almazo, I.** (2006) High-resolution stratigraphy of the Mediterranean outflow contourite system in the Gulf of Cadiz during the late Pleistocene: the impact of Heinrich events. *Mar. Geol.*, **227**, 241–262.

Longhitano, S.G., **Mellere, D.**, **Steel, R.J.** and **Ainsworth, R.B.** (2012) Tidal depositional systems in the rock record: a review and new insights. *Sed. Geol.*, **279**, 2–22.

Longhitano, S.G. and **Nemec, W.** (2005) Statistical analysis of bed-thickness variation in a Tortonian succession of biocalcarenitic tidal dunes, Amantea Basin, Calabria, southern Italy. *Sed. Geol.*, **179**, 195–224.

Martín-Chivelet, J., **Fregenal-Martínez, M.A.** and **Chacón, B.** (2008) Traction structures in contourites. *Dev. Sedimentol.*, **60**, 157–182.

McKee, E.D., **Reynolds, M.A.** and **Baker, C.H., Jr.** (1962) *Laboratory Studies on Deformation in Unconsolidated Sediment*. US Geological Survey Professional Paper, 151.

Mézerais, M.L., **Faugères, J.C.**, **Figueiredo, A.G., Jr.** and **Massé, L.** (1993) Contour current accumulation off the Vema Channel mouth, southern Brazil Basin: pattern of a "contourite fan". *Sediment. Geol.*, **82**, 173–187.

Michard, A., **Saddiqi, O.**, **Chalouan, A.** and **de Lamotte, D.F.** (2008) *Continental Evolution: The Geology of Morocco: Structure, Stratigraphy, and Tectonics of the Africa-Atlantic-Mediterranean Triple Junction*, Vol. **116**. Springer, Berlin.

Miguez-Salas, O. and **Rodríguez-Tovar, F.J.** (2021) Trace fossil analysis of sandy clastic contouritic deposits in the late Miocene Rifian corridor (Morocco): Ichnotaxonomical and palaeoenvironmental insights. *J. Afr. Earth Sci.*, **174**, 104054.

Millot, C. (1999) Circulation in the western Mediterranean Sea. *J. Mar. Syst.*, **20**, 423–442.

Mulder, T. (2011) Gravity processes and deposits on continental slope, rise and abyssal plains. *Dev. Sedimentol.*, **63**, 25–148.

Mutti, E. (1992) *Turbidite Sandstones*. Agip, Istituto di geologia, University di Parma, Parma.

Mutti, E., **Bernoulli, D.**, **Lucchi, F.R.** and **Tinterri, R.** (2009) Turbidites and turbidity currents from alpine 'flysch'to the exploration of continental margins. *Sedimentology*, **56**, 267–318.

Mutti, E. and **Carminatti, M.** (2011) Deep-water sands of the Brazilian offshore basins. In: *AAPG International Conference and Exhibition, Milan, Italy*, pp. 1–42. AAPG Database, Tulsa.

Nelson, C.H., **Baraza, J.** and **Maldonado, A.** (1993) Mediterranean undercurrent sandy contourites, Gulf of Cadiz, Spain. *Sed. Geol.*, **82**(1-4), 103–131.

Owen, G. (1995) Soft-sediment deformation in upper Proterozoic Torridonian sandstones (Applecross formation) at Torridon, Northwest Scotland. *J. Sediment. Res.*, **65**(3a), 495–504.

Owen, G. (1996) Experimental soft-sediment deformation: structures formed by the liquefaction of unconsolidated sands and some ancient examples. *Sedimentology*, **43**, 279–293.

Parker, G. (2008) Transport of gravel and sediment mixtures. In: *Sedimentation Engineering: Processes, Measurements, Modeling, and Practice* (Ed. Garcia, M.H.), pp. 165–251. American Society of Civil Engineering, Reston, VA.

Paulat, M., **Lüdmann, T.**, **Betzler, C.** and **Eberli, G.P.** (2019) Neogene palaeoceanographic changes recorded in a carbonate contourite drift (Santaren Channel, Bahamas). *Sedimentology*, **66**, 1361–1385.

Peakall, J. and **Sumner, E.J.** (2015) Submarine channel flow processes and deposits: a process-product perspective. *Geomorphology*, **244**, 95–120.

Piper, D.J. and **Normark, W.R.** (1983) Turbidite depositional patterns and flow characteristics, navy submarine fan, California Borderland. *Sedimentology*, **30**, 681–694.

Rahmstorf, S. (2006) Thermohaline Ocean circulation. In: *Encyclopedia of Quaternary Sciences* (Ed. Elias, S.A.), Vol. **5**. Elsevier, Amsterdam.

Raudkivi, A.J. (1976) *Loose Boundary Hydraulics*. University of California, Pergamon Press, London. https://doi.org/10.1201/9781003077800

Reading, H.G. (2009) *Sedimentary Environments: Processes, Facies and Stratigraphy*. Blackwell Science Ltd.

Rebesco, M., **Hernández-Molina, F.J.**, **Van Rooij, D.** and **Wåhlin, A.** (2014) Contourites and associated sediments controlled by deep-water circulation processes: state-of-the-art and future considerations. *Mar. Geol.*, **352**, 111–154.

van Rijn, L.C. (1984) Sediment transport, part III: bed forms and alluvial roughness. *J. Hydraul. Eng.*, **110**, 1733–1754.

Rodríguez-Tovar, F.J. and **Aguirre, J.** (2014) Is Macaronichnus an exclusively small, horizontal and unbranched structure? Macaronichnus segregatis degiberti isubsp. Nov. *Spanish J. Palaeontol.*, **29**, 131–142.

Rogerson, M., **Rohling, E.J.**, **Bigg, G.R.** and **Ramirez, J.** (2012) Paleoceanography of the Atlantic-Mediterranean exchange: overview and first quantitative assessment of climatic forcing. *Rev. Geophys.*, **50**, RG2003.

Rohling, E.J., **Marino, G.** and **Grant, K.M.** (2015) Mediterranean climate and oceanography, and the periodic development of anoxic events (sapropels). *Earth Sci. Rev.*, **143**, 62–97.

Roldán, F.J., **Galindo-Zaldívar, J.**, **Ruano, P.**, **Chalouan, A.**, **Pedrera, A.**, **Ahmamou, M.**, **Ruiz-Constan, A.**, **Sanz de Galdeano, C.**, **Benmakhlouf, M.**, **Lopez-Garrido, A.C.**, **Anahnah, F.** and **Gonzalez-Castillo, L.** (2014) Basin evolution associated with curved thrusts: the Prerif ridges in the Volubilis area (Rif cordillera, Morocco). *J. Geodyn.*, **77**, 56–69.

Ryan, W.B.F. and **Hsü, K.J.** (1973) *Initial Reports of the Deep-Sea Drilling Project, 13*. US Govt. Printing Office, Washington, DC.

Sánchez-Leal, R.F., **Bellanco, M.J.**, **Fernández-Salas, L.M.**, **García-Lafuente, J.**, **Gasser-Rubinat, M.**, **González-Pola, C.** and **Sánchez-Garrido, J.C.** (2017) The Mediterranean overflow in the Gulf of Cadiz: A rugged journey. *Sci. Adv.*, **3**, eaao0609.

Sani, F., **Del Ventisette, C.**, **Montanari, D.**, **Bendkik, A.** and **Chenakeb, M.** (2007) Structural evolution of the rides Prerifaines (Morocco): structural and seismic interpretation and analogue modelling experiments. *J. Earth Sci.*, **96**, 685–706.

Seike, K., **Yanagishima, S.I.**, **Nara, M.** and **Sasaki, T.** (2011) Large *Macaronichnus* in modern shoreface sediments: identification of the producer, the mode of formation, and paleoenvironmental implications. *Palaeogeogr. Palaeoclimatol. Palaeoecol.*, **311**, 224–229.

Shanmugam, G. (2010) Slides, slumps, debris flow, and turbidity currents. In: *Ocean Currents: A Derivative of the Encyclopedia of Ocean Sciences*, Vol. **20**, p. 418. Elsevier Academic Press, Boston, Heidelberg, London.

Sierro, F.J. (1985) The replacement of the "Globorotalia menardii" group by the Globorotalia miotumida group: an aid to recognizing the Tortonian-Messinian boundary in the Mediterranean and adjacent Atlantic. *Mar. Micropaleontol.*, **9**(6), 525–535.

Sierro, F.J., **Flores, J.A.**, **Civis, J.**, **Gonza, J.A.** and **France, G.** (1993) Late Miocene globorotaliid event-stratigraphy and biogeography in the NE-Atlantic and Mediterranean. *Mar. Micropaleontol.*, **21**, 143–167.

Sierro, F.J., **Flores, J.A.**, **Zamarreno, I.**, **Vázquez, A.**, **Utrilla, R.**, **Francés, G.** and **Krijgsman, W.** (1999) Messinian pre-evaporite sapropels and precession-induced oscillations in western Mediterranean climate. *Mar. Geol.*, **153**, 137–146.

Sierro, F.J., **Hilgen, F.J.**, **Krijgsman, W.** and **Flores, J.A.** (2001) The Abad composite (SE Spain): a Messinian reference section for the Mediterranean and the APTS. *Palaeogeogr. Palaeoclimatol. Palaeoecol.*, **168**, 141–169.

Sierro, F.J., **Hodell, D.A.**, **Andersen, N.**, **Azibeiro, L.A.**, **Jimenez-Espejo, F.J.**, **Bahr, A.**, **Flores, J.-A.**, **Ausín, B.**, **Rogerson, M.**, **Lozano-Luz, R.**, **Lebreiro, S.M.** and **Hernandez-Molina, F.J.** (2020) Mediterranean overflow over the last 250 kyr: freshwater forcing from the tropics to the ice sheets. *Paleoceanogr. Paleoclimatol.*, **35**(9), e2020PA003931.

Simon, D., **Marzocchi, A.**, **Flecker, R.**, **Lunt, D.J.**, **Hilgen, F.J.** and **Meijer, P.T.** (2017) Quantifying the Mediterranean freshwater budget throughout the late Miocene: new implications for sapropel formation and the Messinian salinity crisis. *Earth Planet. Sci. Lett.*, **472**, 25–37.

Southard, J.B. and **Boguchwal, L.A.** (1990) Bed configuration in steady unidirectional water flows; part 2, synthesis of flume data. *J. Sediment. Res.*, **60**, 658–679.

Stow, D.A.V., **Hernández-Molina, F.J.**, **Llave, E.**, **Bruno, M.**, **García, M.**, **del Rio, V.D.**, **Somoza, L.** and **Brackenridge, R.E.** (2013) The Cadiz Contourite Channel: Sandy contourites, bedforms and dynamic current interaction. *Mar. Geol.*, **343**, 99–114.

Stow, D.A.V., **Hernández-Molina, F.J.**, **Llave, E.**, **Sayago-Gil, M.**, **Díaz del Río, V.** and **Branson, A.** (2009) Bedform-velocity matrix: the estimation of bottom current velocity from bedform observations. *Geology*, **37**, 327–330.

Straume, E.O., **Gaina, C.**, **Medvedev, S.** and **Nisancioglu, K.H.** (2020) Global Cenozoic Paleobathymetry with a focus on the Northern Hemisphere Oceanic Gateways. *Gondwana Res.*, **86**, 126–143.

Streeter, V.L. and **Kestin, J.** (1961) Handbook of fluid dynamics. *J. Appl. Mech.*, **28**(640), 143.

Talling, P.J., **Masson, D.G.**, **Sumner, E.J.** and **Malgesini, G.** (2012) Subaqueous sediment density flows: depositional processes and deposit types. *Sedimentology*, **59**, 1937–2003.

Tulbure, M.A., **Capella, W.**, **Barhoun, N.**, **Flores, J.A.**, **Hilgen, F.J.**, **Krijgsman, W.** and **Yousfi, M.Z.** (2017) Age refinement and basin evolution of the north Rifian corridor (Morocco): no evidence for a marine connection during the Messinian salinity crisis. *Palaeogeogr. Palaeoclimatol. Palaeoecol.*, **485**, 416–432.

Van den Berg, J.H. and **Van Gelder, A.** (1993) A new bedform stability diagram, with emphasis on the transition of ripples to plane bed in flows over fine sand and silt. *Spec. Public. Int. Assoc. Sedimentol.*, **17**, 11–21.

Viana, A.R. (2008) Economic relevance of contourites. *Dev. Sedimentol.*, **60**, 491–510.

Viana, A.R., **Almeida, W.**, **Nunes, M.C.V.** and **Bulhões, E.M.** (2007) The economic importance of contourites. *Geol. Soc. Lond. Spec. Publ.*, **276**, 1–23.

Walker, R.G. (1978) Deep-water sandstone facies and ancient submarine fans: models for exploration for stratigraphic traps. *AAPG Bulletin*, **62**, 932–966.

de Weger, W., **Hernández-Molina, F.J.**, **Flecker, R.**, **Sierro, F.J.**, **Chiarella, D.**, **Krijgsman, W.** and **Manar, M.A.** (2020) Late Miocene contourite channel system reveals intermittent overflow behavior. *Geology*, **48**(12), 1194–1199.

de Weger, W., **Hernández-Molina, F.J.**, **Miguez-Salas, O.**, **de Castro, S.**, **Bruno, M.**, **Chiarella, D.**, **Sierro, F.J.**, **Blackbourn, G.** and **Manar, M.A.** (2021) Contourite depositional system after the exit of a strait: case study from the late Miocene south Rifian corridor, Morocco. *Sedimentology*, **68**, 2996–3032.

Weimer, P. and **Slatt, R.M.** (2004) *Petroleum systems of deepwater settings*. Society of Exploration Geophysicists and European Association of Geoscientists and Engineers. Society of Exploration Geophysicists, Houston.

Wernli, R. (1988) Micropaléontologie du Néogène post-nappes du Maroc septentrional et description systématique des foraminifères planctoniques. *Notes et Mémoires du Service Géologique*, **331**, 270.

Wetzel, A. (2008) Recent bioturbation in the deep South China Sea: a uniformitarian ichnologic approach. *Palaios*, **23**, 601–615.

Wynn, R.B., **Cronin, B.T.** and **Peakall, J.** (2007) Sinuous deep-water channels: genesis, geometry and architecture. *Marine Petrol. Geol.*, **24**, 341–387.

Yalin, M.S. (1977) Mechanics of sediment transport. *Sediment. Geol.*, **15**, 1–53.

Zhang, X., **Zhang, T.**, **Lei, B.**, **Zhang, J.** and **Yong, J.** (2020) A giant sandy sediment drift in early Silurian (Telychian) and its multiple sedimentological prosess. *Marine and Petroleum Geology*, **113**, 104077.